Heteroanionic $LaBrVIO_4$ (VI=Mo, W): Excellence in Both Nonlinear Optical Properties and Photoluminescent Properties

Zixian Jiao [a], Osvaldo Medina Mireles [a], Kevin Ensz [a], Fei Wang [b], Mingli Liang [c], P. Shiv Halasyamani [c], Bingbing Zhang [d], D. Paul. Rillema [a], Jian Wang [a] *

[a] Department of Chemistry and Biochemistry, Wichita State University, Wichita, Kansas 67260, United States

[b] Department of Chemistry, Missouri State University, Springfield, Missouri, 65897, United States

[c] Department of Chemistry, University of Houston, Houston, TX, 77204, United States

[d] College of Chemistry and Environmental Science, Hebei University, Key Laboratory of Analytical Science and Technology of Hebei Province, Baoding 071002, China

Abstract

Five heteroanionic oxybromides, $LaBrMoO_4$, $LaBrWO_4$, $(La_{0.9}Sm_{0.1})BrMoO_4$, $(La_{0.9}Sm_{0.1})BrWO_4$, and $(La_{0.9}Dy_{0.1})BrWO_4$ were grown by a high temperature salt flux method. Millimeter-sized crystals were collected after salt flux was removed by DI water. The crystal structures were accurately determined by single crystal X-ray diffraction. $LaBrMoO_4$ is isostructural to $LaBrWO_4$. The substitution of lanthanum for rare earth elements does not change the crystal structure. $LaBrWO_4$ is the first acentric tungsten-containing compound of the $REBrVIO_4$ (RE=Y, La-Lu; VI=Mo, W) system. The bonding picture of $LaBrWO_4$ was understood by crystal orbital Hamilton population calculations (COHP) and electron localization function (ELF) analysis, which confirmed the uncommon 4+1 coordination of tungsten surrounded by oxygen atoms. Linear optical properties such as bandgaps, infrared spectrum (IR), and birefringence of the title compounds were recorded in this work. $LaBrMoO_4$ exhibits a moderate second harmonic generation (SHG) response of 0.47× KH_2PO_4 (KDP) for incident 1064 nm radiation. $LaBrWO_4$ and $(La_{0.9}Dy_{0.1})BrWO_4$ exhibit superior SHG response of 1.66×KDP and 3.71×KDP for samples for incident 1064 nm radiation, respectively. All measured samples exhibited type-I phase matching behavior. Density function calculations (DFT) verified that the optical properties of $LaBrMoO_4$ and $LaBrWO_4$ are predominantly controlled by $[VIO_5]_{VI=Mo, W}$ units. Via rare earth elements Sm and Dy doping, $LaBrMoO_4$ and $LaBrWO_4$ emit visible lights of

various wavelengths upon UV light excitation. The distortion of lambda (Λ)-shaped one dimensional (1D) $[VIO_5]_{VI=Mo, W}$ strands plays an important role in enhancing nonlinear optical properties and photoluminescent properties within $LaBrWO_4$ and $(La_{0.9}Dy_{0.1})BrWO_4$ compared with $LaBrMoO_4$.

Introduction

Heteroanionic compounds, which constitute two or more different anions, have attracted growing interest due to structural flexibility and emerging physical properties including nonlinear optical (NLO) properties,[1-11] superconducting properties,[12-15] photoluminescent response [16-32] and thermoelectric properties [33-35], etc. Heteroanionic compounds are different from polyanionic compounds, where there are anion-anion interactions existing within polyanionic clusters such as polyanionic $[PO_4]^{3-}$.[29, 33-40] Heteroanionic compounds do not contain direct anion-anion interactions. Heteroanionic compounds can be cataloged into two groups: disordered-heteroanionic compounds and ordered- heteroanionic compounds. The disordered- heteroanionic compounds refer to compounds having two or more anions jointly occupying the same atomic position such as Cd(SeTe),[41] SnO_2:F [42], and $LaFeAsO_{1-x}F_x$.[12] The distinct anions occupy independent atomic positions within the ordered-heteroanionic compounds such as Na_3MoOF_3 ,[43] $LaGaOS_2$,[44] $KBe_2BO_3F_2$,[1] BiCuSeO ,[45] CeZnSbO , [46] etc. The different properties of various anions existing within one crystal lattice greatly enhance the structural flexibility of the heteroanionic compounds. The boundary of heteroanionic compounds was further extended recently via inserting H or C into known compounds such as $NdScSiC_x$[47] and $CeTiGeH_x$.[48]

Oxybromides are compounds constructed by O^{2-} and Br^- as anions. The chemically distinct O^{2-} (ionic size: 126 pm; electronegativity: 3.4) and Br^- (ionic size: 182 pm; electronegativity: 3.0) made most oxybromides as ordered-heteroanionic compounds, [49-78] which results in pliable structural chemistry and fruitful physical phenomenon, such as nonlinear optical properties. [49-78] In this work, we report the crystal structure and growth, electronic structures, chemical bonding pictures, linear and NLO properties, and photoluminescent (PL) properties of $LaBrMoO_4$ and $LaBrWO_4$. $LaBrMoO_4$ was structurally characterized without any properties measurements. $LaBrWO_4$ is isostructural to $LaBrMoO_4$, which was discovered as the first acentric tungsten-contained compound of the $REBrVIO_4$ (RE=Y, La-Lu; VI=Mo, W) system.[54,55,60,79] $LaBrWO_4$ exhibits improved SHG response and PL properties than $LaBrMoO_4$, which was elucidated by

DFT calculations and structural analysis. This work promotes future studies about discovering new NLO and PL materials within the $REHaVIO_4$ (RE=Y, La-Lu; VI=Mo, W; Ha=Cl, Br I) system.

Experimental Details

Synthesis: All reactants were stored in an argon-filed glovebox with an oxygen level below 0.5 ppm. All starting materials were commercial grade and used as received: $LaBr_3$ (Alfa Aesar, 99.9%), La_2O_3 (Alfa Aesar, ≥ 99.9%), MoO_3 (Alfa Aesar, 99.5%), WO_3 (Alfa Aesar, 99.8%), Sm_2O_3 (Fisher Scientific, 99.9%), Dy_2O_3 (Fisher Scientific, 99.9%), NaBr (Fisher Scientific, 99+ %).

The crystals of $LaBrMoO_4$, $LaBrWO_4$, $(La_{0.9}Sm_{0.1})BrMoO_4$, $(La_{0.9}Sm_{0.1})BrWO_4$, and $(La_{0.9}Dy_{0.1})BrWO_4$, were grown by a high temperature salt flux method in a stoichiometric ratio with the aid of $LaBr_3$/NaBr flux (La_2O_3/RE_2O_3/$LaBr_3$/VIO_3(VI=Mo, W)=1-x/x/1/3, X=0.1 for RE=Sm and Dy, x=0 for samples without rare earth elements doping. The chemical reaction follows the equation: (1-x) La_2O_3+ xRE_2O_3 (RE=Sm, Dy) +$LaBr_3$+ $3VIO_3$ (VI=Mo, W) ->$3(La_{1-x}RE_x)BrWIO_4$ (x= 0 or 0.1). A total of 0.4 g reactants were mixed within a glove box with 0.4 g flux covered on the top of the reactants. The molar ratio of $LaBr_3$/NaBr is 1/1. Then the quartz ampoules were sealed under vacuum and placed in a programmable furnace. The bottom of the silica tubes was coated with amorphous carbon (thermal decomposition of acetone) to prevent potential chemical reactions between reactants and silica tubes. The ampules were heated from room temperature to 1093 K in 10 hours and kept at this temperature for 168 hours. Then the furnace was turned off and naturally cooled down to room temperature. The flux was removed by DI water. All products are transparent crystals and stable in air for a long time. The yields of the reactions were about 75% based on La_2O_3. The optical microscope photos of selected crystals of $LaBrMoO_4$ and $LaBrWO_4$ were shown in **Figure S1**. The phase purity of $LaBrMoO_4$, $LaBrWO_4$, $(La_{0.9}Sm_{0.1})BrMoO_4$, $(La_{0.9}Sm_{0.1})BrWO_4$, and $(La_{0.9}Dy_{0.1})BrWO_4$ were verified by powder X-ray diffraction (**Figures S2-S6**).

Single Crystal X-ray Diffraction: Crystals of $LaBrMoO_4$, $LaBrWO_4$ and $(La_{0.9}Dy_{0.1})BrWO_4$ were manually picked up under an optical microscope and mounted to the Rigaku XtaLAB Synergy-I instrument. The data collection was performed at 290 (5) K. The data collection and integration were done by CrysAlis^{Pro} Software (Agilent Technologies, XRD Products; CrysAlis Pro; Agilent Technologies, Inc). The structural solution and refinement were done with Jana2006

[80]. Details of the data collection and structure refinement are provided in **Table 1**. Atomic coordinates and selected bond distances are listed in **Tables S1** and **S2**. There are two independent La atomic positions, La1 and La2, within the asymmetric unitcell of $LaBrWO_4$. The refinement of single crystal X-ray diffraction results of $(La_{0.9}Dy_{0.1})BrWO_4$ revealed that Dy atoms occupy La1 atomic position. The occupancy of La1 and Dy1 are 0.95(1) and 0.05(1), respectively. The refinement of the La2 atomic position found that the occupancy is close to 100%. Hence the empirical formula determined by single crystal X-ray diffraction was $(La_{0.97(1)}Dy_{0.03(1)})BrWO_4$, which was confirmed by Energy-dispersive X-ray spectroscopy analysis (EDS). The EDS results were shown in **Table S3**. EDS results confirmed that the experimentally determined formula of $(La_{0.9}Dy_{0.1})BrWO_4$ sample was $(La_{0.93}Dy_{0.11})BrW_{1.17}O_{2.47}$**.** The PXRD did not detect any impurity peaks (**Figure S6**). Another proof of successfully incorporating Dy elements into $LaBrWO_4$ is the PL properties (*vide infra*). Without rare earth element doping, there were no PL properties detected for $LaBrWO_4$ under UV light irradiation. Hence, we proposed that all rare earth elements were successfully incorporated into the crystal lattice to substitute La atoms. We use the loading compositions, chemical formulas, $(La_{0.9}Sm_{0.1})BrMoO_4$, $(La_{0.9}Sm_{0.1})BrWO_4$, and $(La_{0.9}Dy_{0.1})BrWO_4$, to represent these related rare earth-doped samples. Crystallographic data for $LaBrWO_4$ and $(La_{0.9}Dy_{0.1})BrWO_4$ have been deposited to the Cambridge Crystallographic Data Centre, CCDC, 12 Union Road, Cambridge CB21EZ, UK. Copies of the data can be obtained free of charge by quoting the depository numbers CCDC- 2261483 ($LaBrWO_4$) and CCDC- 2261484 ($(La_{0.9}Dy_{0.1})BrWO_4$).

Table 1. Refined crystallographic parameters of $LaBrWO_4$, $LaBrMoO_4$, and $(La_{0.9}Dy_{0.1})BrWO_4$.

Compound	$LaBrWO_4$	$LaBrMoO_4$	$(La_{0.9}Dy_{0.1})BrWO_4$
Formula weight (g mol^{-1})	466.7	378.7	469.0
Crystal color		colorless	
Temperature		300(5) K	
Radiation, wavelength		Mo-Kα, 0.71073 Å	
Crystal system		Monoclinic	
Space group		*P c* (no.7)	
a(Å)	9.8808 (1)	9.8240 (1)	9.8775 (1)
b(Å)	5.9221 (1)	5.8225 (1)	5.9219 (1)
c(Å)	7.9469 (1)	8.1145 (1)	7.9407 (1)
β (°)	90.0031 (4)	90.0092 (5)	90.0120 (5)
V ($Å^3$)	465.0135 (4)	464.151 (5)	464.480 (6)

Z		4	
D_c (g cm^{-1})	6.67	5.42	6.71
μ (mm^{-1})	42.261	20.278	42.999
F(000)	792	664	793
Flack Parameter	0.085(6)	0.025(8)	0.148(9)
R1, wR2 (I > 2σ(I))	0.0103, 0.0137	0.0112, 0.0158	0.0141, 0.0178
R1, wR2 (all data)	0.0106, 0.0138	0.0114, 0.0159	0.0142, 0.0179

$R_1 = \sum||F_o| - |F_c||/\sum|F_o|$; $wR_2 = [\sum[w(F_o^2 - F_c^2)^2]/\sum[w(F_o^2)^2]]^{1/2}$, and $w = 1/[\sigma^2F_o^2 + (A \cdot P)^2 + B \cdot P]$, $P = (F_o^2 + 2F_c^2)/3$; A and B are weight coefficients.

Lab powder X-ray Diffraction: Powder X-ray diffraction data were recorded at room temperature using a Rigaku Mini Flex 6G diffractometer with copper-Kα radiation (λ =1.5406 Å) in the range 2θ = 10° – 80°, at a scan step of 0.04° with ten seconds exposure time.

Energy-dispersive X-ray spectroscopy analysis (EDS): EDS was employed to verify the compositions of rare earth doped $LaBrMoO_4$ and $LaBrWO_4$ samples. Manually picked crystals of $(La_{0.9}Sm_{0.1})BrMoO_4$, $(La_{0.9}Sm_{0.1})BrWO_4$, and $(La_{0.9}Dy_{0.1})BrWO_4$ samples were transferred to Phenom Pharos G2 Desktop FEG-SEM instrument. The EDS results were summarized in **Table S3**.

UV-Vis Measurements: Diffuse-reflectance spectra were collected at 300K by a PERSEE-T8DCS UV-Vis spectrophotometer equipped with an integration sphere in the wavelength range of 230−850 nm. The reflectance data, R, were collected and converted to the Kubelka-Munk function, $f(R)=(1-R)^2(2R)^{-1}$. Tauc plots, $(KM*E)^2$ and $(KM*E)^{1/2}$, were applied to estimate direct and indirect bandgaps, respectively.

Second Harmonic Measurements: Using the Kurtz and Perry method,[81] powder SHG responses of $LaBrMoO_4$, $LaBrWO_4$ and $(La_{0.9}Dy_{0.1})BrWO_4$ compounds were investigated by a Nd:YAG laser (1064 nm) with various particle sizes, including <20, 20–45, 45–63, 63–75, 75–90, 90–125, and 125–180 μm, 180–250 μm . Polycrystalline KH_2PO_4 (KDP) was also sieved into similar particle sizes for SHG efficiency comparison. A short pass filter was placed in front of the photomultiplier tube to prevent scattered 1064 nm photons from being detected.

Photoluminescent Properties measurements: Photoluminescence measurements were acquired using a Horiba Fluorolog FL3-2iHR fluorescence spectrometer. Fluorescence excitation and emission spectra were recorded of powder samples at room temperature.

TB-LMTO-ASA Calculations: Bonding picture studies of $LaBrWO_4$, including crystal orbital Hamilton population (COHP) and electron localization function (ELF), are calculated using the

tight binding-linear muffin tin orbitals-atomic sphere approximation (TB-LMTO-ASA) program.[82,83] The von-Barth-Hedin exchange potential was employed for the LDA calculations.[82] The radial scalar-relativistic Dirac equation was solved to obtain the partial waves. The density of states and band structures were calculated after converging the total energy on a dense k-mesh of $LaBrWO_4$ (10×20×20 points with 2200 irreducible k-points).

DFT Calculations: The electronic structures and optical properties of $LaBrMoO_4$ and $LaBrWO_4$ were calculated based on ab initio calculations implemented in the CASTEP package through density functional theory (DFT).[84] The Perdew−Burke−Emzerhof (PBE) functional [85] within the generalized gradient approximation (GGA) [86] was adopted to calculate the exchange-correlation potential, with an energy cutoff of 750 eV for $LaBrMoO_4$ and $LaBrWO_4$.. The numerical integration of the Brillouin zone was performed using a Monkhorst−Pack k-point sampling. The k-point separation for each material was set as 0.04 $Å^{-1}$. The geometry optimizations were applied prior to property calculations. Norm-conserving pseudopotentials were employed. The local-density approximation (LDA)+U approach (where U is the Hubbard energy) is adopted to deal with strongly correlated compounds.

Results and discussions

Crystal growth and phase purification

The high temperature solid state method was employed as the major technique to grow crystals of $REBrVIO_4$ (RE=Y, La-Lu; VI=Mo, W) [54,55,60,79] , where $REBr_3$ was used as reactants and flux. Small amounts of impurity were detected after the reaction process of $LaBrMoO_4$ [79]. In this work, we employed a new flux pair of $LaBr_3$/NaBr to grow crystals of $LaBrVIO_4$ (VI=Mo, W) and rare earth-doped samples. The $LaBr_3$/NaBr (molar ratio=1/1) flux was theoretically predicted to have a low eutectic point temperature close to 1023 K.[87] Single phase samples and large crystals of $LaBrVIO_4$ (VI=Mo, W) and rare earth-doped samples were successfully grown by the $LaBr_3$/NaBr flux (**Figures S1-S6**). Hence $REBr_3$/NaBr flux should be a good flux to grow and uncover more compounds within the $REBrVIO_4$ (RE=Y, La-Lu; VI=Mo, W) system.

Crystal Structure

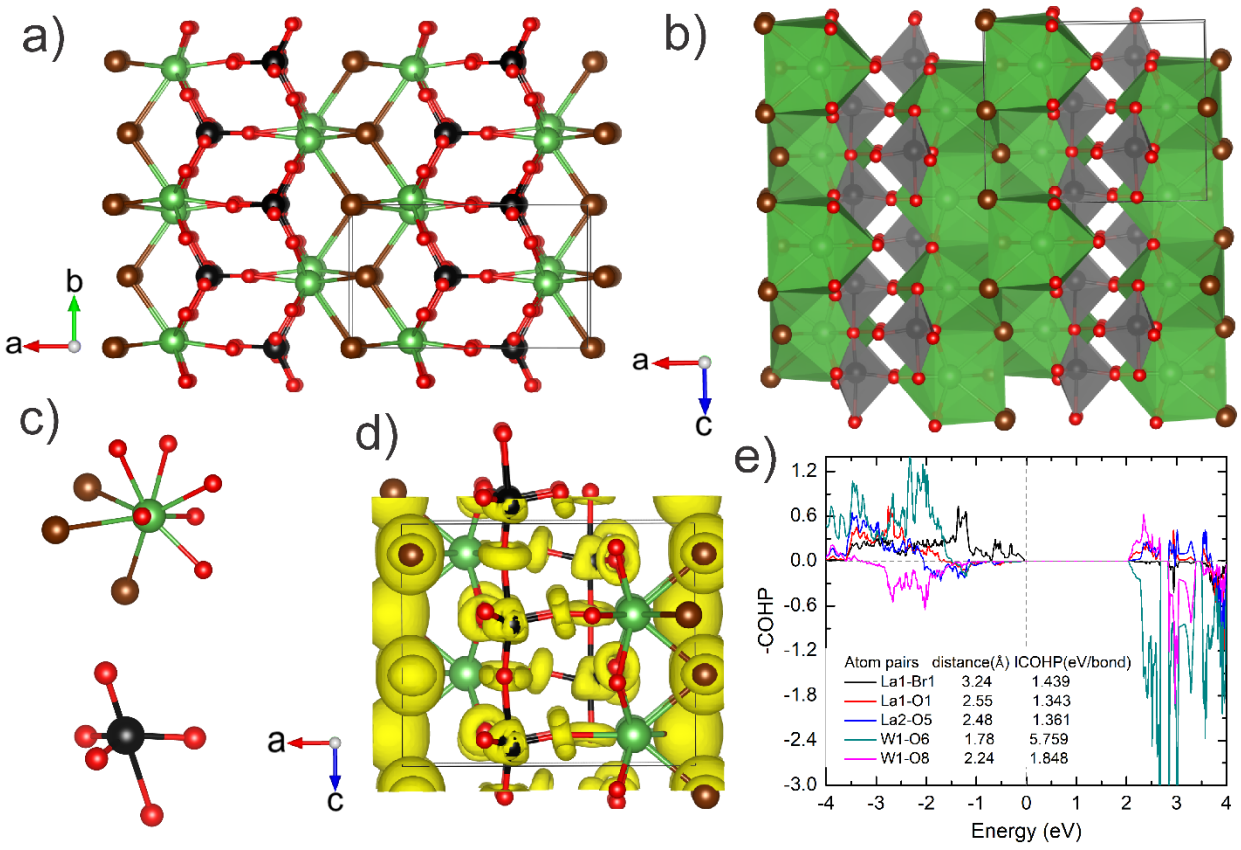

Figure 1. (a) Ball-stick structure of $LaBrWO_4$ viewed along [001] direction; (b) polyhedral structure viewed along [010] direction; (c) a detailed view of [LaO_6Br_3] polyhedral and [WO_5] trigonal bipyramid; (d) 3D isosurfaces of ELF for $LaBrWO_4$ with η=0.60; (e) COHP analyses of the selected La-Br, La-O, and W-O interactions. La: green, W: black, O: red, Br: brown.

$LaBrWO_4$ is isostructural to $LaBrMoO_4$, which belongs to the $REBrVIO_4$ (RE=Y, La-Lu; VI=Mo, W) system.[54,55,60,79] $LaBrWO_4$ is discovered for the first time. The rare earth-doping did not change the crystal structure (**Table 1**). The crystal structure of Dy-doped $LaBrWO_4$ was confirmed by single crystal X-ray diffraction and powder X-ray diffraction (**Table 1, Figure S6**). The selected structure refinement parameters and crystal data for $LaBrMoO_4$, $LaBrWO_4$, and $(La_{0.9}Dy_{0.1})BrWO_4$ are summarized in **Table 1**. The refined atomic coordinates and selected important interatomic distances of $LaBrMoO_4$, $LaBrWO_4$, and $(La_{0.9}Dy_{0.1})BrWO_4$ are summarized in **Table S1 and Table S2**, respectively. Based on the ICSD 2022 database, there are twenty-three compounds reported within the $REBrVIO_4$ (RE=Y, La-Lu; VI=Mo, W) system (**Table S4**).[54,55,60,79] Few interesting observations: 1) there are two structure models reported: acentric *Pc* (two compounds) and centrosymmetric $P\bar{1}$ (twenty-one compounds); 2) There are fourteen Mo-

containing compounds studied versus only nine W-contained compounds. All W-containing compounds crystallize in the centrosymmetric $P\bar{1}$ structure model; 3) All W-containing compounds constitute rare earth elements from Gd to Lu with no light rare earth elements involved such as La and Ce except Y. $LaBrWO_4$ is the first acentric W-contained compound of the $REBrVIO_4$ (RE=Y, La-Lu; VI=Mo, W) system, which exhibits excellent nonlinear optical properties and photoluminescent properties (*vide infra*). To simplify the discussion, $LaBrWO_4$ was selected to present the crystal structure of $LaBrMoO_4$, $LaBrWO_4$, and $(La_{0.9}Dy_{0.1})BrWO_4$.

$LaBrWO_4$ forms in the acentric monoclinic space group *Pc* (no. 7) with unit cell parameters of a = 9.8808(1) Å, b = 5.9221(1) Å, and c = 7.9469(1) Å, and β = 90.0031(4)°. Because β is close to 90°, orthorhombic symmetry was also considered during lattice and space group determination. The R_{int} value of the *b*-unique monoclinic lattice (R_{int} = 0.0306) is noticeably lower than the orthorhombic lattice (R_{int} = 0.0404). The attempts to integrate all diffraction spots including high angle data also resulted in monoclinic lattice. Structural solution and refinement were done with orthorhombic space groups, such as *Pmcm*, *P*2*cm*, and *Pmc*2_1 and all yielded R values higher than 0.10. This is the case for all these three single crystals reported in **Table 1**. Therefore, their structures were eventually refined with the *b*-unique monoclinic lattice and the most satisfying results were obtained in the space group *Pc*, which is consistent with the previous report on $LaBrMoO_4$ and $CeBrMoO_4$.[54] Because of the pseudo-orthorhombic lattice, pseudo-merohedral twinning was observed in all the single crystals. The two twinning domains are oriented by a 180° rotation about ***a***-axis. In addition, because *Pc* is non-centrosymmetric, the absolute structure parameters, or Flack parameters (also listed in Table 1), [88] were also refined by introducing the center-inverted structure as a twinning domain. The Wyckoff sequence of $LaBrWO_4$ is a^{14} with the Pearson symbol *mP28*. There are two distinct La atoms, two distinct W atoms, two distinct Br atoms, and eight distinct S atoms in the asymmetric unit cell of $LaBrWO_4$ with full occupancy. The crystal structure of $LaBrWO_4$ is summarized in **Figures 1a-1c**. The three-dimensional (3D) framework of $LaBrWO_4$ is constructed by two-dimensional (2D) $[LaBrO_4]^{6-}$ strips interlinked via distorted $[WO_5]$ trigonal bipyramids. The distorted $[WO_5]$ trigonal bipyramids connect to each other via apical oxygen atoms to form one-dimensional (1D) strands running along the [001] direction. The 2D $[LaBrO_4]^{6-}$ strips are built by distorted tetracapped trigonal prisms $[LaO_6Br_3]$, where six oxygen atoms and three bromine atoms surround the central La atoms as shown in **Figure 1c**. The intrinsically distorted $[WO_5]$ trigonal

bipyramids are also shown in **Figure 1c**. The crystal structure of $LaBrWO_4$ can also be viewed as constructed by 2D cationic $[LaWO_4]^{1+}$ strips sandwiched by anionic Br- layers as shown in **Figure S7**. The connectivity between two cationic $[LaWO_4]^{1+}$ strips is via La-Br interactions (**Figure S8**).

The La-O interaction within distorted tetracapped trigonal prisms $[LaO_6Br_3]$ fall into a narrow range of 2.468(4)-2.672(5) Å, which are comparable to many oxides such as $Na_3La(AsO_4)_2$(2.415-2.927 Å),[89] $LaTiSbO_6$(2.463 Å),[90] $LaClMoO_4$(2.490-2.633 Å),[91] $LaClWO_4$(2.491-2.547 Å),[16] etc. The bonding pictures of La-O interactions were also studied via ELF simulations coupled with COHP calculations shown in **Figures 1d** and **1e**, respectively. The –ICOHPs for 2.48 Å La-O interaction and 2.55 Å La-O interaction are 1.361 eV/bond and 1.343 eV/bond, respectively (**Figure 1e**). There are also no obvious attractors existing between La and O atoms (**Figure 1d**). Hence, the La-O interactions can be treated as moderately strong ionic interactions. The La-Br interaction within distorted tetracapped trigonal prisms $[LaO_6Br_3]$ are 3.131 (1) - 3.254(1) Å, which are typical for La-Br interactions such as $LaBr_3$ (3.100-3.158 Å),[92] LaOBr (3.293 Å),[93] La_2SbS_5Br (3.115-3.293 Å),[94] etc. The –ICOHPs for the 3.24 Å La-Br interaction are 1.439 eV/bond. The bonding pictures of La-Br interaction are close to La-O interactions, which are both moderately strong ionic interactions.

The W atoms have a 4+1 coordination environment within $LaBrWO_4$, forming distorted trigonal bipyramids (**Figure 1c** bottom). The four shorter W-O interactions fall into the range of 1.759 (4)-1.825 (3) Å. The –ICOHPs for 1.78 Å W-O interaction are 5.759 eV/bond, which exhibits very strong bonding characters (**Figure 1e**). The apical O atoms, which connect to neighbor W atoms to form 1D strands, are separated from the W atom by 2.24-2.25 Å. The 2.24 Å W-O interactions exhibit moderately strong bonding characters, which were verified by –ICOHPs of 1.848 eV/bond. Interestingly, there are also no visible attractors located between W and O atoms as shown in **Figure 1d**. The COHP calculations indicate that the 4+1 coordination environment is true for tungsten atoms within $LaBrWO_4$. The same 4+1 coordination environment for W atoms was also found in $Ce_{10}W_{22}O_{81}$.[95] A previous study shows that the interaction between $[LaO_6Br_3]$ and $[MoO_5]$ within $LaBrMoO_4$ plays an important role in forming this 4+1 coordination environment.[79] The 4+1 coordination environment for W and Mo is uncommon. Some selected Mo- and W-constituted oxybromides are summarized in **Table S5**.[50-61] The four or six coordination environments for Mo and W atoms are the most common. Our study also confirmed that the

distortion degree of 1D [WO_5] strands play a critical role in determining NLO and PL properties (*vide infra*).

Linear Optical properties

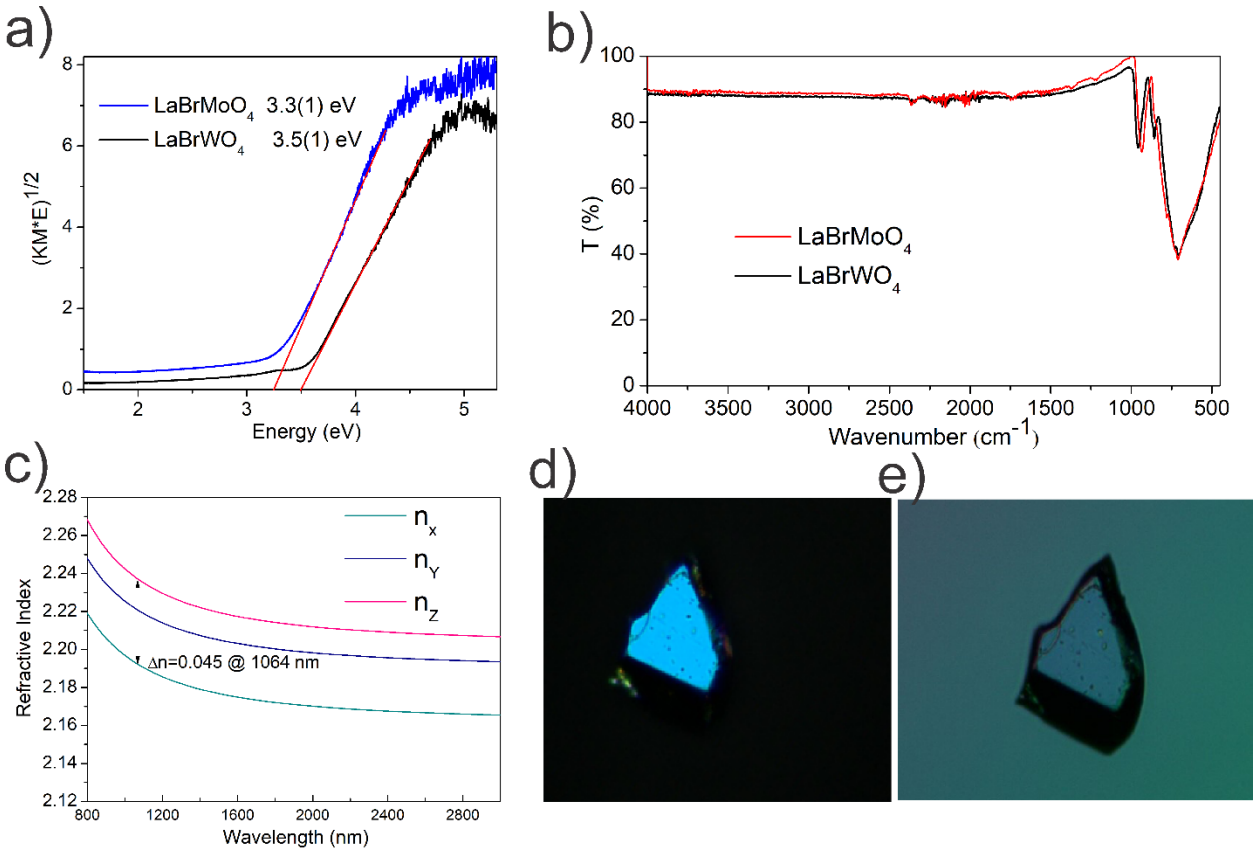

Figure 2. (a) UV-Vis spectroscopy measurements and (b) IR spectrum of $LaBrVIO_4$ (VI=Mo, W). (c) Calculated frequency-dependent refractive indices of $LaBrMoO_4$. (d) Original interference color of $LaBrMoO_4$ crystal in cross-polarized light during birefringence measurements. (e) The photo of $LaBrMoO_4$ crystal after extinction.

The linear optical properties including bandgaps, IR transmission spectroscopy, and birefringence of $LaBrVIO_4$ (VI=Mo, W) were studied and summarized in **Figure 2**. The bandgaps of $LaBrVIO_4$ (VI=Mo, W) were estimated by UV-Vis spectral measurements (**Figure 2a**). Both $LaBrVIO_4$ (VI=Mo, W) were predicated to be indirect bandgap semiconductors (*vide infra*). The indirect bandgaps are 3.3(1) eV and 3.5(1) eV for $LaBrMoO_4$ and $LaBrWO_4$, respectively. The large bandgaps agree well with the colorless nature of $LaBrVIO_4$ (VI=Mo, W) crystals. The reproducibility of bandgap measurements was presented in **Figure S9** and **Figure S10**, which

confirmed the reliability of our bandgap measurement results. The IR spectrum of $LaBrMoO_4$ and $LaBrWO_4$ were recorded and presented in **Figure 2b**, where a high similarity of the IR spectrum was observed for $LaBrMoO_4$ and $LaBrWO_4$. The IR spectrum did not show any intrinsic vibrational absorption of chemical bonds in the wavelength of 2.5–10 μm. The strong absorption peaks appear in the range of 10–20 μm, which can be assigned to the ν (Mo–O) or ν (W-O) vibrations for $LaBrMoO_4$ and $LaBrWO_4$, respectively.[22,58, 96-103] The IR spectrum of $LaBrMoO_4$ and $LaBrWO_4$ is comparable to many tungsten-oxides or molybdenum-oxides such as $CsNa_2Eu_2H_3[Eu_2(H_2O)_7(\alpha\text{-}Si_2W_{18}O_{66})]Cl_2\cdot 30\ H_2O$ [98], $La_3Cl_3[MoO_6]$, [22] and $K_5(W_3O_9F_4)(IO_3)$.[103] The birefringence of $LaBrVIO_4$ (VI=Mo, W) was estimated by both experimental measurements and DFT calculations. For $LaBrMoO_4$, the experimentally estimated birefringence is 0.045, which is measured by a cross-polarizing microscope. The optical path difference was measured to be ~23.6 μm at 1203 nm according to the function of the Michal-Levy charts [104]. As shown in **Figure 2d**, the initial interference color of $LaBrMoO_4$ was identified as third-order blue under orthogonally polarized light. The photo of the $LaBrMoO_4$ crystal after extinction is shown in **Figure 2e**. The experimental measurements of the birefringence of $LaBrMoO_4$ agree well with DFT calculation results, 0.045 and 0.045, respectively (**Figure 2d**). The experimental birefringence of $LaBrWO_4$ is comparable to $LaBrMoO_4$, which is summarized in **Figure S11**. The experimentally measured birefringence of $LaBrWO_4$ is 0.051@1064 nm. $LaBrWO_4$ crystallizes in the monoclinic *Pc* space group. The crystallographic axis is different from the optic axis within $LaBrWO_4$. The angle differences between the crystallographic axis and optic axis along [001] direction and [100] direction are 3.15° and 3.19°, respectively. The moderate birefringence values of $LaBrMoO_4$ and $LaBrWO_4$ account for the type-I phase-matching behavior during SHG measurements (*vide infra*). The birefringence of $LaBrMoO_4$ is close to some oxybromides such as $MB_2O_3F_2$ (M=Sn, Pb) (0.01@1064nm),[105] $Sn_3PO_4F_3$ (0.011@1064nm),[106] $Ba_2B_5O_9Cl$ (0.012@1064nm),[107] $Sn_3B_3O_7F$ (0.031@1064nm),[106] $Pb_3(SeO_3)Br_4$ (0.04@1064nm),[65] $BaAlBO_3F_2$(0.042@1064nm),[108] $[BaF]\cdot[B_2O_3F]$ (0.05@1064nm),[105] etc. The structural complexity can significantly enhance the birefringence of oxybromides such as $Sn_{14}O_{11}Br_6$ (0.265@546 nm), [109] Sn_2PO_4Br (0.303@1064 nm), [108] and $Sn_2B_5O_9Br$ (0.439@546 nm).[70]

Nonlinear Optical properties

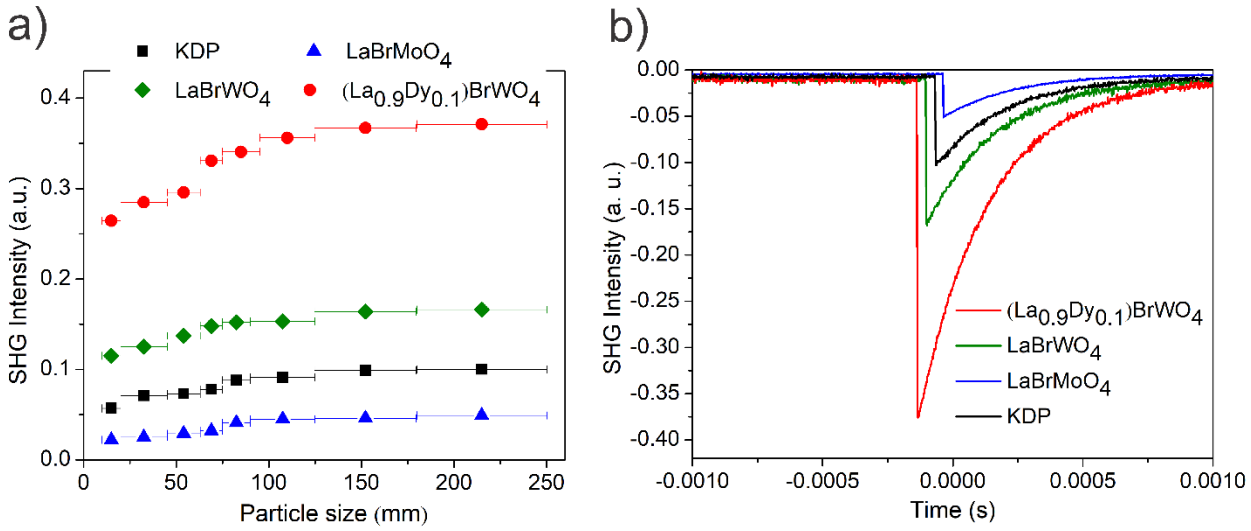

Figure 3. (a) Size-dependent SHG intensities of $LaBrVIO_4$ (VI=Mo, W), $(La_{0.9}Dy_{0.1})BrWO_4$, and the KH_2PO_4 (KDP) reference. (b) The SHG intensity of samples of $LaBrVIO_4$ (VI=Mo, W), $La_{0.9}Dy_{0.1}BrWO_4$, and KDP of particle sizes of 180-250 μm.

The nonlinear optical properties of $LaBrVIO_4$ (VI=Mo, W) and $(La_{0.9}Dy_{0.1})BrWO_4$ are summarized in **Figure 3**. As shown in **Figure 3a**, $LaBrMoO_4$, $LaBrWO_4$, and $(La_{0.9}Dy_{0.1})BrWO_4$ are type-I phase-matching materials for incident 1064 nm radiation, which the SHG response increases with increasing particle size. The SHG response of $LaBrMoO_4$ is 0.47 × KDP for the sample of particle size of 180-250 μm. $LaBrWO_4$ exhibits a much better SHG response, which is 1.66 × KDP. $(La_{0.9}Dy_{0.1})BrWO_4$ exhibits a superior SHG response of ~3.71×KDP. The superior SHG performance of $LaBrWO_4$ and $(La_{0.9}Dy_{0.1})BrWO_4$ are comparable to many previously reported oxybromides such as $Pb_2Ba_3(BO_3)_3Br$ (3.1×KDP),[73] $Sr_5La(BO_3)_4Br$ (2.4×KDP),[69] $NaBa_4(GaB_4O)_2Br_3$(1.1×KDP),[66] $KZn_2BO_3Br_2$ (3.0×KDP),[63] $(K_{2.33}Na_{0.67})(B_6O_{10})Br$ (2.8×KDP),[71] $Sn_2B_5O_9Br$ (2.4×KDP),[70] $Pb_2NbO_2(SeO_3)_2Br$ (1.4×KDP),[72] $Pb_2GaF_2(SeO_3)_2Br$ (4.5×KDP),[72] $Pb_3(SeO_3)Br_4$ (1.0×KDP),[65] etc. A comparison of optical properties between $LaBrVIO_4$ (VI=Mo, W) and selected previously reported oxybromides is tabulated in **Table S6**.[62-78] Even the $LaBrWO_4$ and $LaBrMoO_4$ are isostructural, what is the chemical reason for the superior SHG response of $LaBrWO_4$ compared with $LaBrMoO_4$? The small amounts of dysprosium doping also dramatically enhance the SHG response of $(La_{0.9}Dy_{0.1})BrWO_4$. Understanding how to enhance SHG in NLO materials are critical for pushing this filed forward.[110-119] In addition to SHG response, $LaBrWO_4$ also possesses better PL properties than $LaBrMoO_4$ (vide infra). Our further analysis confirms that

the distorted 1D $[VIO_5]_{VI=Mo, W}$ strands play a critical role in determining the optical properties of $LaBrVIO_4$ (VI=Mo, W) (*vide infra*).

Photoluminescent Properties

The large bandgaps of $LaBrWO_4$ and $LaBrMoO_4$ guarantee their broad optical transmission range. The high stability plus easy to grow large crystals of $LaBrWO_4$ and $LaBrMoO_4$ inspired us to explore more optical applications of $LaBrWO_4$ and $LaBrMoO_4$. The closely related system $REClVIO_4$ (RE=Y, La-Lu; VI= Mo, W) system has demonstrated excellent applications as PL materials.[16-26] In contrast to Cl-containing compounds, the rather soft bromides were thought probably not suitable for PL applications due to the luminescence quenching effect [79]. In this work, good luminescence properties of $LaBrWO_4$ and $LaBrMoO_4$ were achieved via rare earth element doping (**Figure 4**). $LaBrWO_4$ and $LaBrMoO_4$ crystals did not fluoresce at room temperature under UV excitation. Hence, rare earth activators were incorporated into $LaBrWO_4$ and $LaBrMoO_4$ crystals. As shown in **Figure 4a** inert, 0.01 mole Sm^{3+}-doped $LaBrWO_4$ emits bright orange light. Excited by 405 nm light, the predominant emission occurred at 596 nm, arising from the $^4G_{5/2}$->$^6H_{7/2}$ transition. The second most intense emission peak at 647 nm is from $^4G_{5/2}$->$^6H_{9/2}$ transition. The emission peak at 560 nm and 706 nm stems from $^4G_{5/2}$->$^6H_{5/2}$ and $^4G_{5/2}$->$^6H_{11/2}$ transitions, respectively. The Sm^{3+}-doped $LaBrWO_4$ exhibits a very comparable emission spectrum with Sm^{3+}-doped $LaBrMoO_4$ as shown in **Figure 4c**. The Sm^{3+} activator exhibit typical emission spectrum within $LaBrWO_4$ and $LaBrMoO_4$ host lattice, which were observed in many known crystals and glasses.[120,121,122] The Dy^{3+} activators within $LaBrWO_4$ hosting lattice emit yellow-green visible light excited by 405 nm light as shown in **Figure 4b** insert. There are three typical emission peaks found in the emission spectrum of $(La_{0.9}Dy_{0.1})$ $BrWO_4$. The strongest emission peak at 575 nm is from $^4F_{9/2}$->$^6H_{13/2}$ transition. The emission peak at 476 nm comes from $^4F_{9/2}$->$^6H_{15/2}$ transition. The emission peak at 663 nm stems from $^4F_{9/2}$->$^6H_{11/2}$ transition.[123-126] The same activators, Dy^{3+} did not emit any light within $LaBrMoO_4$. The SHG response process originates from nonlinear polarization process. PL response comes from the excited electrons transferring between different energy levels. $LaBrWO_4$ exhibits superior properties than $LaBrWO_4$ for both processes. What is the chemical reason for this difference? Hence, we firstly studied the electronic properties of $LaBrWO_4$ and $LaBrMoO_4$.

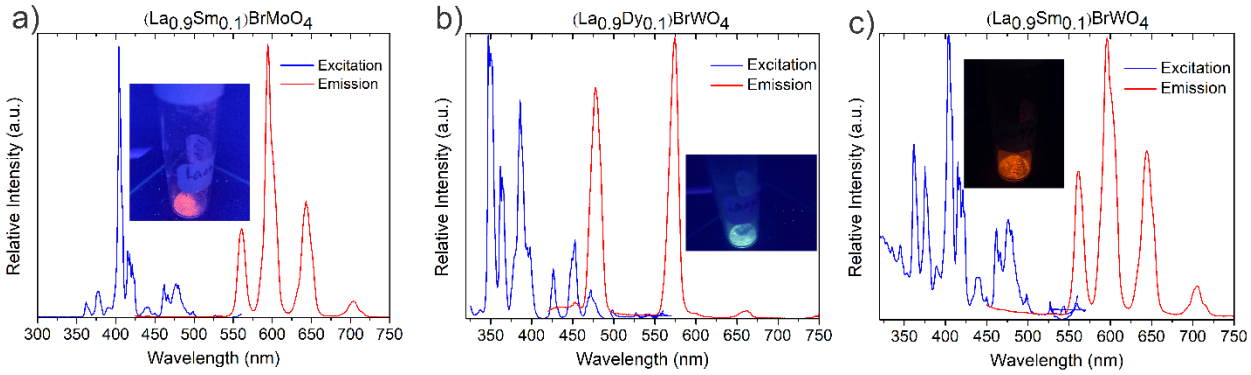

Figure 4. Room-temperature excitation (left, blue) and emission (right, red) spectrum of $(La_{0.9}Sm_{0.1})BrMoO_4$ (a), $(La_{0.9}Dy_{0.1})BrWO_4$ (b), and $(La_{0.9}Sm_{0.1})BrWO_4$ (c). The insert in each figure shows the luminescence of each sample at room temperature under UV light with λ_{exc}=405 nm.

DFT calculations

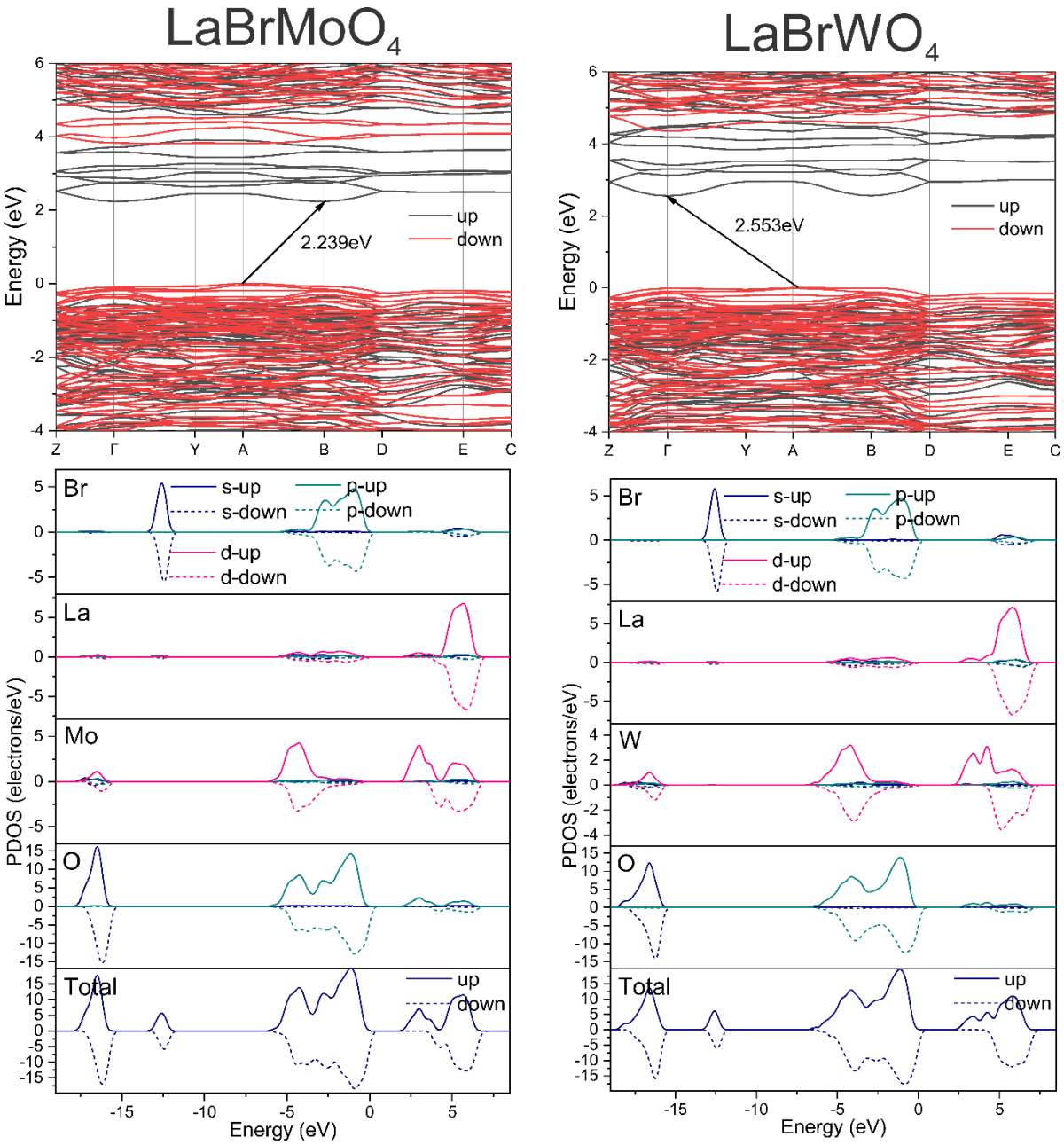

Figure 5. (Left) band structure of $LaBrMoO_4$ (top) and density of states of $LaBrMoO_4$ (bottom). (Right) band structure of $LaBrWO_4$ (top) and density of states (DOS) of $LaBrWO_4$ (bottom). Both spin-up and spin-down states are presented for $LaBrMoO_4$ and $LaBrWO_4$.

The band structures and density of states of $LaBrWO_4$ and $LaBrMoO_4$ are presented in **Figure 5**. To accurately estimate the electronic structure of $LaBrWO_4$ and $LaBrMoO_4$, both the spin-up and spin-down models were turned on [127]. Both $LaBrWO_4$ and $LaBrMoO_4$ are predicated to be indirect bandgap semiconductors. The semiconducting nature of $LaBrWO_4$ and $LaBrMoO_4$ was

also verified by UV-Vis measurements (**Figure 2a**). The charge-balanced formula $[La^{3+}][Br^{-}][W^{6+}][O^{2-}]_4$ can be achieved by assigning a formal charge of 3+ to the La atoms, 6+ to the W atoms, 1- to the Br atoms, and 2- to the O atoms for $LaBrWO_4$. The oxidation state of La and W atoms of +3 and +6, respectively, was validated by bond valence sum calculations [128]. Bond valence sum (BVS) calculations concluded that the BVS of La atoms and W atoms is 2.89 and 6.01, respectively, which suggests La atoms and W atoms with oxidation state of +3 and +6, respectively. The indirect bandgaps for $LaBrWO_4$ and $LaBrMoO_4$ are 2.24 eV and 2.55 eV, respectively, which are smaller than the experimental results. Underestimation of bandgaps of inorganic solids is normal for DFT calculation especially when there are transition metals present.[129] For DOS results, the top of the valance band is mainly contributed by O-2p orbitals and Br-4p orbitals. The orbitals from Mo and La atoms have minimum contributions to the top of the valance band. For the bottom of the conduction band, the Mo-4d orbitals and O-2p orbitals play a dominant role, where contributions from the La-5d orbitals and Br-4p orbitals can be ignored. The La-5d orbitals mainly populate in the interval of 4-6 eV. Since the negligible contributions from La atoms to both top of valance bands and bottom of conduction bands, W-O interactions are expected to play a dominant role in contributing to the NLO and PL properties. Hence, we anticipate that $[MoO_5]$ units dominantly control the optical properties of $LaBrMoO_4$ together with certain contributions from $[LaBr_3O_6]$ units. $LaBrWO_4$ exhibits a very close electronic structure with $LaBrMoO_4$. The W-O interactions, La-Br interactions together with La-O interactions both contribute to the optical properties of $LaBrWO_4$. However, a noticeable difference exists between $LaBrMoO_4$ and $LaBrWO_4$. There is a pseudogap existing around the energy of 4.5 eV for $LaBrMoO_4$. At the same energy level, there are absent of any pseudogaps within $LaBrWO_4$. The electronic structure analysis confirms that the Mo-O interactions and W-O interactions are important in determining the optical properties of $LaBrMoO_4$ and $LaBrWO_4$, respectively.

Structure-Property relationships

The SHG response of $LaBrWO_4$ is about 3.5× $LaBrMoO_4$. $(La_{0.9}Dy_{0.1})BrWO_4$ exhibits superior SHG response, 7.9× $LaBrMoO_4$. $LaBrMoO_4$, $LaBrWO_4$ and $(La_{0.9}Dy_{0.1})BrWO_4$ are isostructural to each other. The ionic sizes for Mo^{6+} and W^{6+} are 0.73 Å and 0.74 Å, respectively.[49] The La-O bond distances and La-Br bond distances within $LaBrMoO_4$ and $LaBrWO_4$ are comparable to each other (**Table 2**). The electronic analysis confirms that the $[MoO_5]$ and $[WO_5]$ units play a major

role in contributing to the NLO properties of $LaBrMoO_4$ and $LaBrWO_4$, respectively. The bridging connection between two adjacent [MoO_5] and [WO_5] units is decreasing from $LaBrMoO_4$ to $LaBrWO_4$ and $(La_{0.9}Dy_{0.1})BrWO_4$ (**Table 2**). The Mo1-O8 interaction within $LaBrMoO_4$ is 2.341(3) Å. The W1-O8 interaction within $LaBrWO_4$ is 2.245 (3) Å. The $(La_{0.9}Dy_{0.1})BrWO_4$ possesses shortest W1-O8 interaction of 2.241(4) Å. The shrinkage of W-O interaction results in the distortion of 1D [WO_5] strands. As shown in **Table 2**, the distortion of 1D $[VIO_5]_{VI=Mo,\ W}$ strands is measured by VI-O-VI bond angles. As summarized in **Table 2**, the W1-O8-W1 angle is 158.8(3) ° within $LaBrWO_4$, which is smaller than Mo1-O8-Mo1 angle of $LaBrWO_4$ (161.4(2) °). The W2-O7-W2 bond angles are 158.1(4)° and 158.7(4) ° for $LaBrWO_4$ and $(La_{0.9}Dy_{0.1})BrWO_4$, respectively. The importance of the distortion degree of structure motifs contributing to NLO materials has been reported in many works.[111-119,130-132] The 1D $[VIO_5]_{VI=Mo,\ W}$ strands are similar to many well-known lambda (Λ)-shaped building units in many NLO optical materials such as $K_5Nb_3O_3F_{14}\cdot H_2O$,[133] $K_{10}(Nb_2O_2F_9)_3F$,[134] $K_{10}(Nb_2O_2F_9)_3I_2$,[135] β-$Ba_2[VO_2F_2(IO_3)_2]IO_3$,[136] $K_5(W_3O_9F_4)(IO_3)$,[103] $Sn_2B_5O_9Br$,[70] etc., where the distortion of lambda (Λ)-shaped building units play an critical role in dominating NLO properties. A summary of compounds constituting lambda (Λ)-shaped building units is tabulated in **Table S7**.[70,103,133-137] The $LaBrWO_4$ can also host more rare earth elements than $LaBrMoO_4$, which exhibits intriguing PL properties. The larger bandgap of $LaBrWO_4$ compared to $LaBrMoO_4$, which originates from the contributions from W atoms to the bottom of the conduction band, accounts for better PL properties. The chemical features of W atoms further separated the conduction band and valance band, which results in larger bandgap within $LaBrWO_4$ compared with $LaBrMoO_4$. The larger bandgap of $LaBrWO_4$ can host rare earth elements such as Dy, which has complex energy transitions.[138]

Table 2. The comparison of bandgaps and structural parameters between $LaBrMoO_4$, $LaBrWO_4$ and $(La_{0.9}Dy_{0.1})BrWO_4$.

	$LaBrMoO_4$	$LaBrWO_4$	$(La_{0.9}Dy_{0.1})BrWO_4$*
E_a / eV	3.3(1)	3.5(1)	3.7(1)
Dominant units contributing to NLO properties	[MoO_5]	[WO_5]	[WO_5]

La-O distances/ Å	2.459(3)-2.693(4)	2.468(4)- 2.672(5)	2.459(9)-2.676(8)
La-Br distances/ Å	3.155(1)-2.232(2)	3.131 (1)- 3.254(1)	3.119(1)-3.259(2)
VI-O distances/ Å	Mo1-O8: 2.341(3)	W1-O8: 2.245(3)	W1-O8: 2.241(4)
	Mo2-O7: 2.379(3)	W2-O7: 2.251(4)	W2-O7: 2.232(5)
VI-O-VI bond angels/ °	Mo1-O8-Mo1:161.4(2)	W1-O8-W1: 158.8(3)	W1-O8-W1: 158.5(4)
	Mo2-O7-Mo2: 156.0(2)	W2-O7-W2: 158.1(4)	W2-O7-W2: 158.7(4)

*due to the isostructural nature between $LaBrWO_4$ and $(La_{0.9}Dy_{0.1})BrWO_4$, the electronic structure of $(La_{0.9}Dy_{0.1})BrWO_4$ is assumed the same with $LaBrWO_4$.

Conclusions:

Millimeter-sized crystals of five ordered-heteroanionic oxybromides, $LaBrMoO_4$, $LaBrWO_4$, $(La_{0.9}Sm_{0.1})BrMoO_4$, $(La_{0.9}Sm_{0.1})BrWO_4$, and $(La_{0.9}Dy_{0.1})BrWO_4$ were grown by a high temperature flux method with the aid of $LaBr_3$/NaBr. $LaBr_3$/NaBr flux was removed by water rinsing. $LaBrMoO_4$, $LaBrWO_4$ and rare earth-doped samples are isostructural and crystallize in the acentric $LaBrMoO_4$ structure type. The 3D framework of $LaBrWO_4$ is constructed by two-dimensional (2D) $[LaBrO_4]^{6-}$ strips interlinked via distorted 1D $[WO_5]$ strands. The unusual 4+1 coordination environment of tungsten surrounded by oxygen atoms was verified by bonding picture studies. $LaBrMoO_4$ and $LaBrWO_4$ were revealed as indirect bandgap semiconductors by DFT calculations. The bandgaps measured by UV-Vis are 3.3(1) eV and 3.5(1) eV for $LaBrMoO_4$ and $LaBrWO_4$, respectively. $LaBrMoO_4$, $LaBrWO_4$, and $(La_{0.9}Dy_{0.1})BrWO_4$ are good candidates for NLO application due to high SHG response ($LaBrMoO_4$: 0.47×KDP; $LaBrWO_4$: 1.66×KDP; $(La_{0.9}Dy_{0.1})BrWO_4$: 3.71×KDP), type-I phase-matching behavior, high ambient stability, and easy-growth of crystals. Through rare earth elements replacing La atoms, $LaBrMoO_4$, and $LaBrWO_4$ emit various visible lights upon UV lights excitation. The DFT calculations coupled with structural analysis elucidate that the distortion of lambda (Λ)-shaped 1D $[VIO_5]_{VI=Mo, W}$ strands accounts for the enhanced SHG and PL properties of $LaBrWO_4$ compared to $LaBrMoO_4$. This work demonstrates the importance of distortion of basic building units contributing to the optical properties of oxybromides and indicates the potential presence of more multifunctional materials within the $REHaVIO_4$ (RE=Y, La-Lu; VI=Mo, W; Ha=Cl, Br I) system.

ASSOCIATED CONTENTS

Supporting Information

The refined crystallographic data, microscope photo of crystals, lab powder X-ray diffraction results, UV-Vis results and Tauc plot, structure plots, EDS results, experimentally measured birefringence.

Acknowledgments

This research is supported by National Science Foundation (DMR-2316811). J. W thanks Prof. Andrew Swindle from Department of Geology, Wichita State University for allowing the access to SEM-EDS measurements. J. W also thanks Prof. Conggang Li from Tianjin University of Technology, China for measuring the birefringence. PSH and ML thank the Welch Foundation (Grant E-1457) and the NSF (DMR-2002319) for support. F. W acknowledges NSF MRI 2117129 for funding the single crystal X-ray diffractometer.

Corresponding author

Jian Wang jian.wang@wichita.edu

Notes

The authors declare no competing financial interest.

References

[1]. Xia, Y.; Chen, C.; Tang, D.; Wu, B. New Nonlinear Optical Crystals for UV and VUV Harmonic Generation. *Adv. Mater.* **1995**, *7* (1), 79–81. https://doi.org/10.1002/adma.19950070118.

[2]. Oyeka, E. E.; Winiarski, M. J.; Świątek, H.; Balliew, W.; McMillen, C. D.; Liang, M.; Sorolla, M., 2nd; Tran, T. T. $Ln_2(SeO_3)_2(SO_4)(H_2O)_2$ (Ln=Sm, Dy, Yb): A Mixed-Ligand

Pathway to New Lanthanide(III) Multifunctional Materials Featuring Nonlinear Optical and Magnetic Anisotropy Properties. *Angew. Chem. Int. Ed Engl.* **2022**, *61* (48), e202213499. https://doi.org/10.1002/anie.202213499.

[3]. Hu, C.; Cheng, M.; Jin, W.; Han, J.; Yang, Z.; Pan, S. A Cation-Driven Approach toward Deep-Ultraviolet Nonlinear Optical Materials. *Research (Wash. D.C.)* **2023**, *6*, 0053. https://doi.org/10.34133/research.0053.

[4]. Wang, R.; Guo, Y.; Zhang, X.; Xiao, Y.; Yao, J.; Huang, F. $Sr_5Ga_8O_3S_{14}$: A Nonlinear Optical Oxysulfide with Melilite-Derived Structure and Wide Band Gap. *Inorg. Chem.* **2020**, *59* (14), 9944–9950. https://doi.org/10.1021/acs.inorgchem.0c01111.

[5]. Cheng, Y.; Wu, H.; Yu, H.; Hu, Z.; Wang, J.; Wu, Y. Rational Design of a Promising Oxychalcogenide Infrared Nonlinear Optical Crystal. *Chem. Sci.* **2022**, *13* (18), 5305–5310. https://doi.org/10.1039/d2sc00099g.

[6]. Shi, Y.-F.; Wei, W.-B.; Wu, X.-T.; Lin, H.; Zhu, Q.-L. Recent Progress in Oxychalcogenides as IR Nonlinear Optical Materials. *Dalton Trans.* **2021**, *50* (12), 4112–4118. https://doi.org/10.1039/d1dt00222h.

[7]. Wang, J.; Cheng, Y.; Wu, H.; Hu, Z.; Wang, J.; Wu, Y.; Yu, H. Sr3 [$SnOSe_3$][CO_3]: A Heteroanionic Nonlinear Optical Material Containing Planar π-Conjugated [CO_3] and Heteroleptic [$SnOSe_3$] Anionic Groups. *Angew. Chem. Int. Ed Engl.* **2022**, *61* (21), e202201616. https://doi.org/10.1002/anie.202201616.

[8]. Wang, R.; Liang, F.; Liu, X.; Xiao, Y.; Liu, Q.; Zhang, X.; Wu, L.-M.; Chen, L.; Huang, F. Heteroanionic Melilite Oxysulfide: A Promising Infrared Nonlinear Optical Candidate with a Strong Second-Harmonic Generation Response, Sufficient Birefringence, and Wide Bandgap. *ACS Appl. Mater. Interfaces* **2022**, *14* (20), 23645–23652. https://doi.org/10.1021/acsami.2c04422.

[9]. Liu, H.; Song, Z.; Wu, H.; Hu, Z.; Wang, J.; Wu, Y.; Yu, H. [Ba_2F_2] [$Ge_2O_3S_2$]: An Unprecedented Heteroanionic Infrared Nonlinear Optical Material Containing Three Typical Anions. *ACS Mater. Lett.* **2022**, *4* (9), 1593–1598. https://doi.org/10.1021/acsmaterialslett.2c00485.

[10]. Qiu, H.; Cai, W.; Yang, Z.; Liu, Y.; Mutailipu, M.; Pan, S. Tetrafluoroborate-Monofluorophosphate $(NH_4)_3[PO_3F]$ $[BF_4]$: First Member of Oxyfluoride with B-F and P-F Bonds. *ACS Org. Inorg.* Au **2021**, *1 (1),* 6–10. https://doi.org/10.1021/acsorginorgau.1c00018.

[11]. Bai, S.; Zhang, X.; Zhang, B.; Li, L.; Wang, Y. SrAlB3O6F2: A Fluoroaluminoborate with $[Al_2B_6O_{14}F_4]$ Units and Large Birefringence. *Inorg. Chem.* **2021**, *60 (13),* 10006–10011. https://doi.org/10.1021/acs.inorgchem.1c01298.

[12]. Kamihara, Y.; Watanabe, T.; Hirano, M.; Hosono, H. Iron-Based Layered Superconductor $La[O_{(1-x)}\ F_{(x)}]FeAs$ (x = 0.05-0.12) with T(c) = 26 K. *J. Am. Chem. Soc.* **2008**, *130* (11), 3296–3297. https://doi.org/10.1021/ja800073m.

[13]. Takahashi, H.; Soeda, H.; Nukii, M.; Kawashima, C.; Nakanishi, T.; Iimura, S.; Muraba, Y.; Matsuishi, S.; Hosono, H. Superconductivity at 52 K in Hydrogen-Substituted $LaFeAsO_{(1-x)}H_x$ under High Pressure. *Sci. Rep.* **2015**, *5 (1),* 7829. https://doi.org/10.1038/srep07829.

[14]. Johrendt, D.; Pöttgen, R. Pnictide oxides: a new class of high-Tc superconductors. *Angew. Chem. Int. Ed.* **2008**, *47*, 4782–4784; https://doi.org/10.1002/anie.200801818.

[15]. Baranets, S.; Darone, G. M.; Bobev, S. Structural Diversity among Multinary Pnictide Oxides: A Minireview Focused on Semiconducting and Superconducting Heteroanionic Materials. *Z. Kristallogr. Cryst. Mater.* **2022**, *237* (1–3), 1–26. https://doi.org/10.1515/zkri-2021-2079.

[16]. Brixner, L. H.; Chen, H. Y.; Foris, C. M. Structure and Luminescence of the Orthorhombic $LnWO_4Cl$-Type Rare Earth Halo Tungstates. J. *Solid State Chem.* **1982**, *45 (1),* 80–87. https://doi.org/10.1016/0022-4596(82)90293-6.

[17]. Ayer, G. B.; Klepov, V. V.; Smith, M. D.; Hu, M.; Yang, Z.; Martin, C. R.; Morrison, G.; Zur Loye, H.-C. $BaWO_2F_4$: A Mixed Anion X-Ray Scintillator with Excellent Photoluminescence Quantum Efficiency. *Dalton Trans*. **2020**, *49 (31),* 10734–10739. https://doi.org/10.1039/d0dt02184a.

[18]. Schustereit, T.; Netzsch, P.; Höppe, H. A.; Hartenbach, I. Green Light: On YCl[WO_4] as Host Material for Luminescence Active Tb^{3+} Cations: Green Light: On YCl[WO_4] as Host Material for Luminescence Active Tb^{3+} Cations. *Z. Anorg. Allg. Chem.* **2018**, *644* (24), 1749–1753. https://doi.org/10.1002/zaac.201800322.

[19]. Hartenbach, I.; Strobel, S.; Schleid, T.; Krämer, K. W.; Dorhout, P. K. Chloride Derivatives of LanthanideOrtho-Oxomolybdates: 1. Structural Comparison, Magnetic Properties, and Luminescence of The LnCl[MoO_4] Representatives with the Smaller Lanthanides (Ln= Sm-Lu). *Z. Anorg. Allg. Chem.* **2009**, *635 (6–7),* 966–975. https://doi.org/10.1002/zaac.200801380.

[20]. Schleid, T.; Strobel, S.; Dorhout, P. K.; Nockemann, P.; Binnemans, K.; Hartenbach, I. YF[MoO_4] and YCl[MoO_4]: Two Halide Derivatives of Yttrium Ortho-Oxomolybdate: Syntheses, Structures, and Luminescence Properties. *Inorg. Chem.* **2008**, *47 (9),* 3728–3735. https://doi.org/10.1021/ic702350p.

[21]. Brixner, L. H.; Chen, H. -y.; Foris, C. M. Structure and Luminescence of the Monoclinic $LnWO_4Cl$-Type Rare Earth Halo Tungstates. *Mater. Res. Bull.* . **1982**, *17* (12), 1545–1556. https://doi.org/10.1016/0025-5408(82)90211-2.

[22]. Dorn, K. V.; Blaschkowski, B.; Netzsch, P.; Höppe, H. A.; Hartenbach, I. Blue Excitement: The Lanthanide(III) Chloride Oxidomolybdates(VI) $Ln_3Cl_3[MoO_6]$ (Ln = La, Pr, and Nd) and Their Spectroscopic Properties. *Inorg. Chem.* **2019**, *58 (13),* 8308–8315. https://doi.org/10.1021/acs.inorgchem.9b00098.

[23]. Schustereit, T.; Schleid, T.; Höppe, H. A.; Kazmierczak, K.; Hartenbach, I. Chloride Derivatives of Lanthanoid (III) Ortho-Oxidotungstates(VI) with the Formula LnCl[WO_4] (Ln=Gd–Lu): Syntheses, Crystal Structures and Spectroscopic Properties. J. *Solid State Chem*. **2015**, *226,* 299–306. https://doi.org/10.1016/j.jssc.2015.01.035.

[24]. Charles, N.; Saballos, R. J.; Rondinelli, J. M. Structural Diversity from Anion Order in Heteroanionic Materials. *Chem. Mater*. **2018**, *30 (10),* 3528–3537. https://doi.org/10.1021/acs.chemmater.8b01336.

[25]. Ahn, C. W.; Jo, J. H.; Choi, J. S.; Hwang, Y. H.; Kim, I. W.; Kim, T. H. Heteroanionic Lead-free Double-perovskite Halides for Bandgap Engineering. *Adv. Eng. Mater.* **2023**, *25 (1)*, 2201119. https://doi.org/10.1002/adem.202201119.

[26]. Machida, K. Synthesis and Materials Design for Heteroanion Compounds. *IOP Conf. Ser.: Mater. Sci. Eng.* **2011**, *18*. 052001. https://doi.org/10.1088/1757-899X/18/5/052001.

[27]. Chen, H.; McClain, R.; He, J.; Zhang, C.; Olding, J. N.; Dos Reis, R.; Bao, J.-K.; Hadar, I.; Spanopoulos, I.; Malliakas, C. D.; He, Y.; Chung, D. Y.; Kwok, W.-K.; Weiss, E. A.; Dravid, V. P.; Wolverton, C.; Kanatzidis, M. G. Antiferromagnetic Semiconductor $BaFMn_{0.5}Te$ with Unique Mn Ordering and Red Photoluminescence. *J. Am. Chem. Soc*. **2019**, *141 (43),* 17421–17430. https://doi.org/10.1021/jacs.9b09382.

[28]. Li, J.; Chen, Z.; Saha, S.; Utterback, J. K.; Aubrey, M. L.; Yuan, R.; Weaver, H. L.; Ginsberg, N. S.; Chapman, K. W.; Filip, M. R.; Karunadasa, H. I. Zwitterions in 3D Perovskites: Organosulfide-Halide Perovskites. *J. Am. Chem. Soc*. **2022**, *144 (49),* 22403–22408. https://doi.org/10.1021/jacs.2c09382.

[29]. Harada, J. K.; Charles, N.; Poeppelmeier, K. R.; Rondinelli, J. M. Heteroanionic Materials by Design: Progress toward Targeted Properties. *Adv. Mater*. **2019**, *31 (19),* e1805295. https://doi.org/10.1002/adma.201805295.

[30]. Holland, M.; Charles, N.; Rondinelli, J. M.; Poeppelmeier, K. R. Reconstructive Transitions from Rotations of Rigid Heteroanionic Polyhedra. *J. Am. Chem. Soc*. **2016**, *138 (36)*, 11882–11889. https://doi.org/10.1021/jacs.6b06813.

[31]. Hirai, D.; Yajima, T.; Nishio-Hamane, D.; Kim, C.; Akiyama, H.; Kawamura, M.; Misawa, T.; Abe, N.; Arima, T.-H.; Hiroi, Z. "visible" 5d Orbital States in a Pleochroic Oxychloride. *J. Am. Chem. Soc*. **2017**, *139 (31),* 10784–10789. https://doi.org/10.1021/jacs.7b05128.

[32]. Dorn, K. V.; Blaschkowski, B.; Förg, K.; Netzsch, P.; Höppe, H. A.; Hartenbach, I. Prism inside: Spectroscopic and Magnetic Properties of the Lanthanide(III) Chloride Oxidotungstates (VI) $Ln_3Cl_3[WO_6]$ (Ln = La – Nd, Sm – Tb): Prism inside: Spectroscopic and Magnetic Properties of the Lanthanide(III) Chloride Oxidotungstates(VI)$Ln_3Cl_3[WO_6]$

(Ln= La - Nd, Sm - Tb). *Z. Anorg. Allg. Chem.* ***2017***, *643 (21),* 1642–1648. https://doi.org/10.1002/zaac.201700247.

[33]. Zhang, C.; He, J.; McClain, R.; Xie, H.; Cai, S.; Walters, L. N.; Shen, J.; Ding, F.; Zhou, X.; Malliakas, C. D.; Rondinelli, J. M.; Kanatzidis, M. G.; Wolverton, C.; Dravid, V. P.; Poeppelmeier, K. R. Low Thermal Conductivity in Heteroanionic Materials with Layers of Homoleptic Polyhedra. *J. Am. Chem. Soc*. **2022**, *144 (6),* 2569–2579. https://doi.org/10.1021/jacs.1c10284.

[34]. McClain, R.; Malliakas, C. D.; Shen, J.; Wolverton, C.; Kanatzidis, M. G. In Situ Mechanistic Studies of Two Divergent Synthesis Routes Forming the Heteroanionic BiOCuSe. *J. Am. Chem. Soc*. **2021**, *143 (31*), 12090–12099. https://doi.org/10.1021/jacs.1c03947.

[35]. Hiramatsu, H.; Yanagi, H.; Kamiya, T.; Ueda, K.; Hirano, M.; Hosono, H. Crystal Structures, Optoelectronic Properties, and Electronic Structures of Layered Oxychalcogenides MCuOCh (M = Bi, La; Ch = S, Se, Te): Effects of Electronic Configurations of M^{3+} Ions. *Chem. Mater*. **2008**, *20 (1),* 326–334. https://doi.org/10.1021/cm702303r.

[36]. Clarke, S. J.; Adamson, P.; Herkelrath, S. J. C.; Rutt, O. J.; Parker, D. R.; Pitcher, M. J.; Smura, C. F. Structures, physical properties, and chemistry of layered oxychalcogenides and oxypnictides. *Inorg. Chem.* **2008**, *47*, 8473–8486; https://doi.org/10.1021/ic8009964.

[37]. Harada, J. K.; Poeppelmeier, K. R.; Rondinelli, J. M. Predicting the Structure Stability of Layered Heteroanionic Materials Exhibiting Anion Order. *Inorg. Chem*. **2019**, *58 (19),* 13229–13240. https://doi.org/10.1021/acs.inorgchem.9b02077.

[38]. Zapp, N.; Oehler, F.; Bertmer, M.; Auer, H.; Sheptyakov, D.; Ritter, C.; Kohlmann, H. Aliovalent Anion Substitution as a Design Concept for Heteroanionic Ruddlesden–Popper Hydrides. *Chem. Commun. (Camb.)* **2022**, *58 (93),* 12971–12974. https://doi.org/10.1039/d2cc04356d.

[39]. Kageyama, H.; Hayashi, K.; Maeda, K.; Attfield, J. P.; Hiroi, Z.; Rondinelli, J. M.; Poeppelmeier, K. R. Expanding Frontiers in Materials Chemistry and Physics with Multiple Anions. *Nat. Commun*. **2018**, *9 (1),* 772. https://doi.org/10.1038/s41467-018-02838-4.

[40]. Masquelier, C.; Croguennec, L. Polyanionic (Phosphates, Silicates, Sulfates) Frameworks as Electrode Materials for Rechargeable Li (or Na) Batteries. *Chem. Rev.* **2013**, *113 (8),* 6552–6591. https://doi.org/10.1021/cr3001862.

[41]. Selvaraj, S. C.; Gupta, S.; Caliste, D.; Pochet, P. Passivation Mechanism in CdTe Solar Cells: The Hybrid Role of Se. *Appl. Phys. Lett.* **2021**, *119 (6),* 062105. https://doi.org/10.1063/5.0058290.

[42]. Karaman, T.; Sherwani, A. ur R.; Can, M. M.; Shawuti, S.; Kaneko, S. Synthesis and Optical Analyses of Fluorine Doped Tin Oxide (SnO_2) Nanoparticles. *Eur. Phys. J. Appl. Phys*. **2021**, *95 (2),* 20402. https://doi.org/10.1051/epjap/2021210034.

[43]. Brink, F. J.; Norén, L.; Goossens, D. J.; Withers, R. L.; Liu, Y.; Xu, C.-N. A Combined Diffraction (XRD, Electron and Neutron) and Electrical Study of $Na_3MoO_3F_3$. *J. Solid State Chem* . ***2003***, *174 (2),* 450–458. https://doi.org/10.1016/s0022-4596(03)00303-7.

[44]. Jaulmes, S. Oxysulfure de Gallium et de Lanthane $LaGaOS_2$. *Acta Crystallogr B Struct Sci* **1978**, *34 (8),* 2610–2612. https://doi.org/10.1107/s0567740878008705.

[45]. Kholodkovskaya, L. N.; Akselrud, L. G.; Kusainova, A. M.; Dolgikh, V. A.; Popovkin, B. A. BiCuSeO: Synthesis and Crystal Structure. *Mater. Sci. For.* **1993**, *133–136,* 693–696. https://doi.org/10.4028/www.scientific.net/msf.133-136.693.

[46]. Liu, J.; Wang, J.; Wang, C.-L.; Xia, S.-Q. $Ce_{1-x}Sr_xZnSbO$: New Thermoelectric Materials Formed between Intermetallics and Oxides. *J. Alloys Compd.* **2016**, *688,* 849–853. https://doi.org/10.1016/j.jallcom.2016.07.235.

[47]. Mahon, T.; Gaudin, E.; Villesuzanne, A.; Chevalier, B.; Tencé, S. Effect of Carbon Insertion on the Structural and Magnetic Properties of NdScSi. *Inorg. Chem.* **2019,** *58 (22),* 15255–15268. https://doi.org/10.1021/acs.inorgchem.9b02260.

[48]. Mahon, T.; Tencé, S.; Pöttgen, R.; Chevalier, B.; Gaudin, E. Study of the Structural Transition and Hydrogenation of CeTiGe. *J. Alloys Compd*. **2019**, *805,* 701–708. https://doi.org/10.1016/j.jallcom.2019.07.104.

[49]. Shannon, R. D. Revised Effective Ionic Radii and Systematic Studies of Interatomic Distances in Halides and Chalcogenides. *Acta Cryst A.* ***1976***, *32 (5),* 751–767. https://doi.org/10.1107/s0567739476001551.

[50]. Leclaire, A. A Novel Mo(V) Monophosphate with Bromine and Mixed Valent Lead and a PbO Double Bond: $Pb^{2+}(Pb^{4+}O)Br(Mo^{5+}O)_2(PO_4)_3$. *Solid State Sci.* **2006**, *8 (6),* 660–664. https://doi.org/10.1016/j.solidstatesciences.2006.01.012.

[51]. Pakhomova, A. S.; Krivovichev, S. V. Tricaesium Dimolybdate(VI) Bromide. *Acta Crystallogr E Struct Rep Online* **2009**, *65 (12),* i87–i87. https://doi.org/10.1107/s1600536809046297.

[52]. Steiner, U.; Reichelt, W.; Böttcher, P.; Däbritz, S. Synthese, Eigenschaften Und Kristallstruktur von $Cu_3Mo_8O_{23}X_2$(X = Cl, Br, I). *Z. Anorg. Allg. Chem.* **1999**, *625 (1),* 160–166. https://doi.org/10.1002/(sici)1521-3749(199901)625:1<160::aid-zaac160>3.0.co;2-s.

[53]. Schustereit, T.; Schleid, T.; Hartenbach, I. The Non-Centrosymmetric Crystal Structure of Molybdenum(VI) Oxide Bromide MoO_2Br_2. *Z. Anorg. Allg. Chem*. **2011**, *637 (9),* 1159–1161. https://doi.org/10.1002/zaac.201100042.

[54]. Hartenbach, I.; Henning, H.; Schleid, T.; Schustereit, T.; Strobel, S. Syntheses, Crystal Structures, and Twinning of the Isotypic Rare-Earth Metal BromideOrtho-Oxidomolybdates $LaBrMoO_4$ and $CeBrMoO_4$. *Z. Anorg. Allg. Chem.* **2013**, *639 (2),* 347–353. https://doi.org/10.1002/zaac.201200433.

[55]. Schustereit, T.; Henning, H.; Schleid, T.; Hartenbach, I. Syntheses and Crystal Structures of the Bromide-Derivatized Lanthanoid(III) Ortho-Oxomolybdates(VI) $LnBr[MoO_4]$ (Ln = Pr, Nd, Sm, Gd– Lu). *Z. Naturforsch. B.* **2013**, *68 (5–6),* 616–624. https://doi.org/10.5560/znb.2013-3083.

[56]. Mayer, I.; Zolotov, S.; Kassierer, F. The Crystal Structure of Rare Earth and Yttrium Oxybromides. *Inorg. Chem.* **1965**, *4*, 1637– 1639, DOI: 10.1021/ic50033a022.

[57]. Müller, U. Wolframtetrabromidoxid, $WOBr_4$. *Acta Crystallogr C Cryst Struct Commun* ***1984***, 40 (6), 915–917. https://doi.org/10.1107/s0108270184006259.

[58]. Zheng, Y.-Q.; Peters, K.; von Schnering, H. G. The mixed valence tungsten (IV, V) compound $Na[W_2O_2Br_6]$. *Z. Anorg. Allg. Chem*. **1998**, *624 (9),* 1415–1418. https://doi.org/10.1002/(sici)1521-3749(199809)624:9<1415::aid-zaac1415>3.0.co;2-5.

[59]. Schieweling, M.; Daniels, J.; Beck, J. Mixed valence tungsten (IV, V) compounds with layered structures (part IV): Syntheses, crystal structures, and conductivity of $BiX_2[W_2O_2X_6]$ (X= cl, Br). *Z. Anorg. Allg. Chem*. **2012**, *638 (11),* 1820–1826. https://doi.org/10.1002/zaac.201200227.

[60]. Schustereit, T.; Schleid, T.; Hartenbach, I. Syntheses and Crystal Structures of the Rare-Earth Metal(III) Bromide Ortho -Oxidotungstates(VI) with the Formula $REBr[WO_4]$ (RE = Y, Gd–Yb). *Solid State Sci*. **2015**, *48,* 218–224. https://doi.org/10.1016/j.solidstatesciences.2015.08.013.

[61]. Beck, J. Ein polymeres Tellur-Kation durch Oxidation von Tellur mit Wolframbromiden. *Angew. Chem.* ***1991***, *103 (9),* 1149–1151. https://doi.org/10.1002/ange.19911030915.

[62]. Yu, P.; Wu, L.-M.; Zhou, L.-J.; Chen, L. Deep-Ultraviolet Nonlinear Optical Crystals: $Ba_3P_3O_{10}X$ (X = Cl, Br). *J. Am. Chem. Soc*. **2014**, *136 (1),* 480–487. https://doi.org/10.1021/ja411272y.

[63]. Yang, G.; Gong, P.; Lin, Z.; Ye, N. A $Zn_2BO_3X_2$(A = K, Rb, NH4; X = Cl, Br): New Members of KBBF Family Exhibiting Large SHG Response and the Enhancement of Layer Interaction by Modified Structures. *Chem. Mater.* **2016**, *28 (24),* 9122–9131. https://doi.org/10.1021/acs.chemmater.6b04272.

[64]. Gong, Y.-P.; Hu, C.-L.; Ma, Y.-X.; Mao, J.-G.; Kong, F. $Pb_2Cd\ (SeO_3)_2X_2$ (X = Cl and Br): Two Halogenated Selenites with Phase Matchable Second Harmonic

Generation. *Inorg. Chem. Front.* **2019**, *6 (11),* 3133–3139. https://doi.org/10.1039/c9qi00936a.

[65]. Wang, X.; Jiang, X.; Liu, H.; Yang, L.; Lin, Z.; Hu, Z.; Meng, X.; Chen, X.; Qin, J. $Pb_3(SeO_3)Br_4$: A New Nonlinear Optical Material with Enhanced SHG Response Designedviaan Ion-Substitution Strategy. *Dalton Trans.* **2018**, *47 (6),* 1911–1917. https://doi.org/10.1039/c7dt04443g.

[66]. Kong, F.; Hu, C.-L.; Liang, M.-L.; Mao, J.-G. $Pb_4(OH)_4(BrO_3)_3(NO_3)$: An Example of SHG Crystal in Metal Bromates Containing π-Conjugated Planar Triangle. *Inorg. Chem*. **2016**, *55 (2)*, 948–955. https://doi.org/10.1021/acs.inorgchem.5b02523.

[67]. Yu, H.; Pan, S.; Wu, H.; Yang, Z.; Dong, L.; Su, X.; Zhang, B.; Li, H. Effect of Rigid Units on the Symmetry of the Framework: Design and Synthesis of Centrosymmetric $NaBa_4(B_5O_9)_2F_2Cl$ and Noncentrosymmetric $NaBa_4(AlB_4O_9)_2Br_3$. *Cryst. Growth Des* **2013**, *13 (8),* 3514–3521. https://doi.org/10.1021/cg4004774.

[68]. Wen, M.; Su, X.; Wu, H.; Lu, J.; Yang, Z.; Pan, S. $NaBa_4(GaB_4O_9)_2X_3$ (X = Cl, Br) with NLO-Active GaO_4 Tetrahedral Unit: Experimental and Ab Initio Studies. *J. Phys. Chem. C* **2016**, *120 (11),* 6190–6197. https://doi.org/10.1021/acs.jpcc.6b00265.

[69]. Yuan, B.; Wu, H.; Hu, Z.; Wang, J.; Wu, Y.; Yu, H. Deep Ultraviolet-Transparent Materials with Strong Second-Harmonic Response. *Chem. Mater*. **2022**, *34 (17),* 8004–8012. https://doi.org/10.1021/acs.chemmater.2c01922.

[70]. Guo, J.; Cheng, S.; Han, S.; Yang, Z.; Pan, S. $Sn_2B_5O_9Br$ as an Outstanding Bifunctional Material with Strong Second-harmonic Generation Effect and Large Birefringence. *Adv. Opt. Mater*. **2021**, *9 (5),* 2001734. https://doi.org/10.1002/adom.202001734.

[71]. Han, S.; Wang, Y.; Pan, S.; Dong, X.; Wu, H.; Han, J.; Yang, Y.; Yu, H.; Bai, C. Noncentrosymmetric versus Centrosymmetric: Influence of the Na_+ Substitution on Structural Transition and Second-Harmonic Generation Property. *Cryst. Growth Des*. **2014**, *14 (4),* 1794–1801. https://doi.org/10.1021/cg4019103.

[72]. Zhao, H.; Gong, P.; Zhang, X.; Lin, Z.; Hu, Z.; Wu, Y. Selenite Bromide Nonlinear Optical Materials $Pb_2GaF_2(SeO_3)_2Br$ and $Pb_2NbO_2(SeO_3)_2Br$: Synthesis and Characterization. *Dalton Trans*. **2020**, *49 (40),* 14046–14051. https://doi.org/10.1039/d0dt02514c.

[73]. Jing, Q.; Dong, X.; Yang, Z.; Pan, S. Synthesis and Optical Properties of the First Lead Borate Bromide with Isolated BO3Groups: $Pb_2Ba_3(BO_3)_3Br$. *Dalton Trans*. **2015**, *44 (38),* 16818–16823. https://doi.org/10.1039/c5dt02652k.

[74]. Li, Y.; Zhang, D.; Liu, L.; Zhang, W.; Zhang, J.; Cong, Y.; Li, X.; Halasyamani, P. S. $Cs_2CdV_2O_6Cl_2$ and $Cs_3CdV_4O_{12}Br$: Two New Non-Centrosymmetric Oxyhalides Containing d^0 and d^{10} Cations and Exhibiting Second Harmonic Generation Activity. *Dalton Trans*. **2019**, *48 (28),* 10642–10651. https://doi.org/10.1039/c9dt02099c.

[75]. Luo, M.; Song, Y.; Liang, F.; Ye, N.; Lin, Z. Pb_2BO_3Br: A Novel Nonlinear Optical Lead Borate Bromine with a KBBF-Type Structure Exhibiting Strong Nonlinear Optical Response. *Inorg. Chem. Front*. **2018**, *5 (4),* 916–921. https://doi.org/10.1039/c8qi00026c.

[76]. Liu, L.; Zhang, B.; Halasyamani, P. S.; Zhang, W. $Pb_2TiFO(SeO_3)_2Br$: A New Polar Compound with the Strongest Second Harmonic Generation in the Selenite Bromide Family. *J. Mater. Chem. C* **2021**, *9 (20)*, 6491–6497. https://doi.org/10.1039/d1tc00663k.

[77]. Yang, M.; Shi, Z.-H.; Yao, W.-D.; Guo, S.-P. Second-Harmonic-Generation-Active Oxyhalides: $CuSb_2O_3X$ (X = Cl, Br). *Inorg. Chem*. **2022**, *61 (1)*, 42–46. https://doi.org/10.1021/acs.inorgchem.1c03588.

[78]. Chen, X.; Jo, H.; Ok, K. M. Lead Mixed Oxyhalides Satisfying All Fundamental Requirements for High-performance Mid-infrared Nonlinear Optical Materials. . *Angew. Chem. Int. Ed.* **2020**, *59 (19)*, 7514–7520. https://doi.org/10.1002/anie.202002291.

[79]. Schleid, T.; Hartenbach, I. On Halide Derivatives of Rare-Earth Metal(III) Oxidomolybdates(VI) and -Tungstates(VI). *Z. Kristallogr. Cryst. Mater.* **2016**, *231 (8)*, 449–466. https://doi.org/10.1515/zkri-2016-1974.

[80]. Petricek, V.; Dusek, M.; Palatinus, L. Crystallographic Computing System JANA2006: General Features. *Z. Kristallogr.* **2014,** *229,* 345 – 352. https://doi.org/10.1515/zkri-2014-1737.

[81]. Kurtz, S. K.; Perry, T. T. A Powder Technique for the Evaluation of Nonlinear Optical Materials. *J. Appl. Phys*. **1968**, *39 (8),* 3798–3813. https://doi.org/10.1063/1.1656857.

[82]. Jepsen, O.; Burkhardt, A.; Andersen, O. *The Program TB-LMTO-ASA*; Version4.7, Max-Planck; Stuttgart, Germany, **1999**.

[83]. Barth, U. von.; Hedin, L. A local exchange-correlation potential for the spin polarized case. i. *J. Phys. C: Solid State Phys.***1972**, *5*, 1629–1642.

[84]. Pfrommer, B. G.; Côté, M.; Louie, S. G.; Cohen, M. L. Relaxation of Crystals with the Quasi-Newton Method. *J. Comput. Phys*. **1997**, *131 (1)*, 233–240. https://doi.org/10.1006/jcph.1996.5612.

[85]. Adamo, C.; Barone, V. Toward Reliable Density Functional Methods without Adjustable Parameters: The PBE0 Model. *J. Chem. Phys.* **1999**, *110*, 6158, DOI: 10.1063/1.478522

[86]. Perdew, J. P.; Burke, K.; Ernzerhof, M. Generalized gradient approximation made simple. *Phys. Rev. Lett.* **1996**, *77*, 3865−3868. https://doi.org/10.1103/PhysRevLett.77.3865

[87]. Pilarek, B.; Salamon, B.; Kapała, J. Calculation and Optimization of $LaBr_3$–MBr (Li–Cs) Phase Diagrams by CALPHAD Method. *Calphad* **2014**, *47*, 211–218. https://doi.org/10.1016/j.calphad.2014.10.005.

[88]. Flack, H. D. On enantiomorph-polarity estimation, *Acta Cryst.,* **1983**, *A39*, 876-881. https://doi.org/10.1107/S0108767383001762.

[89]. Bdey, S.; Savvin, S. N.; Bourguiba, N. F.; Núñez, P. Synthesis, Crystal Structure and Na^+ Transport in $Na_3La(AsO_4)_2$. *J. Solid State Chem*. **2022**, *305* , 122644. https://doi.org/10.1016/j.jssc.2021.122644.

[90]. Xie, Y.; Geng, X.; Hu, Z.; Zhou, Z.; Zhou, L.; Zhao, Y.; Chen, J.; Chen, W.; Gong, N.; Deng, B.; Yu, R. Synthesis and Photoluminescence Properties of Novel Orange-Emitting

Sm^{3+}-Activated $LaTiSbO_6$ Phosphors for WLEDs. *Opt. Laser Technol*. **2022**, *147* , 107605. https://doi.org/10.1016/j.optlastec.2021.107605.

[91]. Hartenbach, I.; Schleid, T.; Strobel, S.; Dorhout, P. K. Chloride Derivatives of Lanthanide Ortho-Oxomolybdates:, 3. Crystal Structures, Spectroscopic Studies, and Magnetic Properties of the $LnCl[MoO_4]$ Representatives with the Large Lanthanides (Ln = La, Ce, Pr). *Z. Anorg. Allg. Chem*. **2010**, *636 (7)*, 1183–1189. https://doi.org/10.1002/zaac.200900572.

[92]. Krämer, K.; Schleid, T.; Schulze, M.; Urland, W.; Meyer, G. Three Bromides of Lanthanum: $LaBr_2$, La_2Br_5, and $LaBr_3$. *Z. Anorg. Allg. Chem*. **1989**, *575 (1)*, 61–70. https://doi.org/10.1002/zaac.19895750109.

[93]. Limburg, H.-J.; Hölsä, J.; Porcher, P.; Herzog, G.; Starick, D.; Wulff, H. Evolution of the Crystal Field Effects in (La, Gd)OBr: Eu^{3+} Series. *J. Solid State Chem*. **1992**, *98 (2),* 404–414. https://doi.org/10.1016/s0022-4596(05)80251-8.

[94]. Gout, D.; Jobic, S.; Evain, M.; Brec, R. Synthesis, Structure and Optical Properties of New Lanthanide-Based Derivatives Ln_2SbS_5Br (Ln=La, Ce). *Solid State Sci.* **2001**, *3 (1–2),* 223–234. https://doi.org/10.1016/s1293-2558(00)01111-0.

[95]. Barker, R. S.; Radosavljevic Evans, I. Structural Characterization of $RE_{10}W_{22}O_{81}$ Rare-Earth Tungstates (RE = Ce, Nd). *Acta Crystallogr. B*. **2008**, *64* (Pt 6), 708–712. https://doi.org/10.1107/S0108768108033430.

[96]. Zhang, M.; Lian, Z.; Wang, Y.; Pan, S. Nonlinear optical and self-activated luminescent properties of $A_2W_3O_{10}$ (A = Rb and Cs). *RSC Adv.* **2016**, *6*, 39234-39239, DOI: 10.1039/C6RA03407A

[97]. Ni, L.; Hussain, F.; Spingler, B.; Weyeneth, S.; Patzke, G. R. Lanthanoid-Containing Open Wells–Dawson Silicotungstates: Synthesis, Crystal Structures, and Properties. *Inorg. Chem*. **2011**, *50 (11),* 4944–4955. https://doi.org/10.1021/ic2001943.

[98]. Ni, L.; Spingler, B.; Weyeneth, S.; Patzke, G. R. Trilacunary Keggin-Type POMs as Versatile Building Blocks for Lanthanoid Silicotungstates. *Eur. J. Inorg. Chem.* **2013**, *2013,* 1681–1692. https://doi.org/10.1002/ejic.201201186.

[99]. Chen, X.; Chang, X.; Zang, H.; Wang, Q.; Xiao, W. Hydrothermal Synthesis and Structural Characterization of a Novel NLO Compound, $La(MoO_2)(OH)(IO_3)_4$. *J. Alloys Compd*. **2005**, *396 (1–2),* 255–259. https://doi.org/10.1016/j.jallcom.2004.12.012.

[100]. Chang, S.; Qi, Y.; Wang, E.; Li, Y.; Jin, H. A Novel Dimeric Polyoxotungstate Decorated by 3d-4f Atoms: $K_4LaH[As_2W_{20}CuO_{67}(H_2O)_3]Cl_2 \cdot 22.5H_2O$. *J. Cluster Sci*. **2007**, *18 (4),* 781–796. https://doi.org/10.1007/s10876-007-0131-z.

[101]. Xue, G.; Vaissermann, J.; Gouzerh, P. Cerium(III) Complexes with Lacunary Polyoxotungstates. Synthesis and Structural Characterization of a Novel Heteropolyoxotungstate Based on α-$[SbW_9O_{33}]^{9-}$ Units. *J. Cluster Sci*. **2002**, *13 (3),* 409–421. https://doi.org/10.1023/a:1020555116986.

[102]. Lin, J.; Liu, Q.; Yue, Z.; Diefenbach, K.; Cheng, L.; Lin, Y.; Wang, J.-Q. Expansion of the Structural Diversity of F-Element Bearing Molybdate Iodates: Synthesis, Structures, and Optical Properties. *Dalton Trans*. **2019**, *48 (15),* 4823–4829. https://doi.org/10.1039/c8dt05120h.

[103]. Wu, C.; Lin, L.; Jiang, X.; Lin, Z.; Huang, Z.; Humphrey, M. G.; Halasyamani, P. S.; Zhang, C. $K_5(W_3O_9F_4)(IO_3)$: An Efficient Mid-Infrared Nonlinear Optical Compound with High Laser Damage Threshold. *Chem. Mater*. **2019**, *31 (24),* 10100–10108. https://doi.org/10.1021/acs.chemmater.9b03214.

[104]. Zhao, W.; Jiao, J.; She, Y.; Liang, F.; Ye, N.; Hu, Z.; Wu, Y.; Li, C. Tailored Ordered Structures with Functional Units of Distorted $[NbO_6]$ and Antiparallel $[GeO_4]$ for Enhanced Birefringence in Germanate Crystal. *Adv. Opt. Mater.* **2022**, *10,* 2201704. https://doi.org/10.1002/adom.202201704

[105]. Zhang, B.; Tikhonov, E.; Xie, C.; Yang, Z.; Pan, S. Prediction of Fluorooxoborates with Colossal Second Harmonic Generation (SHG) Coefficients and Extremely Wide Band

Gaps: Towards Modulating Properties by Tuning the BO_3 /BO_3 F Ratio in Layers. *Angew. Chem. Int. Ed.* **2019**, *58 (34),* 11726–11730. https://doi.org/10.1002/anie.201905558.

[106]. Guo, J.; Tudi, A.; Han, S.; Yang, Z.; Pan, S. Sn_2PO_4I: An Excellent Birefringent Material with Giant Optical Anisotropy in Non π-conjugated Phosphate. *Angew. Chem. Int. Ed.* **2021**, *60 (47),* 24901–24904. https://doi.org/10.1002/anie.202111604.

[107]. Guo, J.; Tudi, A.; Han, S.; Yang, Z.; Pan, S. $Sn_2B_5O_9Cl$: A Material with Large Birefringence Enhancement Activated Prepared via Alkaline-earth-metal Substitution by Tin. *Angew. Chem. Int. Ed.* **2019**, *58 (49)*, 17675–17678. https://doi.org/10.1002/anie.201911187.

[108]. Li, R. On the Calculation of Refractive Indices of Borate Crystals Based on Group Approximation. *Z. Kristallogr. Cryst. Mater*. **2013**, 130729000230000. https://doi.org/10.1524/zkri.2013.1628.

[109]. Lu, Z.; Zhang, F.; Tudi, A.; Yang, Z.; Li, Z.; Pan, S. $Sn_{14}O_{11}Br_6$: A Promising Birefringent Material with a [$Sn_{14}O_{11}Br_6$] Layer. *J. Mater. Chem. C* **2021**, *9* (22), 7103–7109. https://doi.org/10.1039/D0TC05942K

[110]. Cropek, C.; Ji, B.; Sarkar, A.; Wang, F.; Syed, T. H.; Wei, W.; Guo, S.-P.; Wang, J. Revisiting Two Thiophosphate Compounds Constituting d^0 Transition Metal $HfP_2S_6$and d^{10} Transition Metal α-$Ag_4P_2S_6$ as Multifunctional Materials for Combining Second Harmonic Generation Response and Photocurrent Response. *CrystEngComm* **2023**, *25* (7), 1175–1185. https://doi.org/10.1039/D2CE01576E

[111]. Ji, B.; Wang, F.; Wu, K.; Zhang, B.; Wang, J. D6 versus D10, Which Is Better for Second Harmonic Generation Susceptibility? A Case Study of $K_2TGe_3Ch_8$ (T = Fe, Cd; Ch = S, Se). *Inorg. Chem.* **2023**, *62 (1)*, 574–582. https://doi.org/10.1021/acs.inorgchem.2c03852.

[112]. Cropek, C.; Nguyen, V.; Chhetri, S. K.; Hu, J.; Guo, S.; Wang, J. Synthesis, Crystal and Electronic Structures, Nonlinear Optical Properties, and Magnetic Properties of Two

Thiophosphates: $KInP_2S_7$ and $KCrP_2S_7$. *Crystals.* **2022**, *12 (11)*, 1505. https://doi.org/10.3390/cryst12111505.

[113]. Bardelli, S.; Ye, Z.; Wang, F.; Zhang, B.; Wang, J. Synthesis, Crystal and Electronic Structures, and Nonlinear Optical Properties of $Y_4Si_3S_{12}$. *Z. Anorg. Allg. Chem*. **2022**, *648, e202100388* . https://doi.org/10.1002/zaac.202100388.

[114]. Nguyen, V.; Ji, B.; Wu, K.; Zhang, B.; Wang, J. Unprecedented Mid-Infrared Nonlinear Optical Materials Achieved by Crystal Structure Engineering, a Case Study of $(KX)P_2S_6$ (X = Sb, Bi, Ba). *Chem. Sci*. **2022**, *13 (9)*, 2640–2648. https://doi.org/10.1039/d1sc06849k.

[115]. Hou, F.; Mei, D.; Zhang, Y.; Liang, F.; Wang, J.; Lu, J.; Lin, Z.; Wu, Y. $SrZnSnSe_4$: A Quaternary Selenide with Large Second Harmonic Generation and Birefringence. *J. Alloys Compd*. **2022**, *904* , 163944. https://doi.org/10.1016/j.jallcom.2022.163944.

[116]. Ji, B.; Wu, K.; Chen, Y.; Wang, F.; Rossini, A. J.; Zhang, B.; Wang, J. $Ba_6(Cu_xZ_y)Sn_4S_{16}$ (Z = Mg, Mn, Zn, Cd, in, Bi, Sn): High Chemical Flexibility Resulting in Good Nonlinear-Optical Properties. *Inorg. Chem.* **2022**, *61 (5)*, 2640–2651. https://doi.org/10.1021/acs.inorgchem.1c03773.

[117]. Wang, W.; Mei, D.; Wen, S.; Wang, J.; Wu, Y. Complex Coordinated Functional Groups: A Great Genes for Nonlinear Optical Materials. *Chin. Chem. Lett*. **2022**, *33 (5),* 2301–2315. https://doi.org/10.1016/j.cclet.2021.11.089.

[118]. Ji, B.; Guderjahn, E.; Wu, K.; Syed, T. H.; Wei, W.; Zhang, B.; Wang, J. Revisiting Thiophosphate $Pb_3P_2S_8$: A Multifunctional Material Combining a Nonlinear Optical Response and Photocurrent Response. *Phys. Chem. Chem. Phys.* **2021**, *23 (41)*, 23696–23702. https://doi.org/10.1039/d1cp03624f.

[119]. Cicirello, G.; Wu, K.; Wang, J. Synthesis, Crystal Structure, Linear and Nonlinear Optical Properties of Quaternary Sulfides $Ba_6(Cu_2X)Ge_4S_{16}$ (X=Mg, Mn, Cd). *J. Solid State Chem*. **2021**, *300* , 122226. https://doi.org/10.1016/j.jssc.2021.122226.

[120]. Guo, H.; Devakumar, B.; Vijayakumar, R.; Du, P.; Huang, X. A Novel Sm^{3+} Singly Doped $LiCa_3ZnV_3O_{12}$ Phosphor: A Potential Luminescent Material for Multifunctional Applications. *RSC Adv.* **2018**, *8 (58)*, 33403–33413. https://doi.org/10.1039/c8ra07329e.

[121]. Prasad, V. R.; Damodaraiah, S.; Babu, S.; Ratnakaram, Y. C. Structural, Optical and Luminescence Properties of Sm^{3+} and Eu^{3+} Doped Calcium Borophosphate Phosphors for Reddish-Orange and Red Emitting Light Applications. *J. Lumin.* **2017**, *187*, 360–367. https://doi.org/10.1016/j.jlumin.2017.03.050.

[122]. Chahar, S.; Taxak, V. B.; Dalal, M.; Singh, S.; Khatkar, S. P. Structural and Photoluminescence Investigations of Sm^{3+} Doped BaY_2ZnO_5 Nanophosphors. *Mater. Res. Bull.* **2016**, *77*, 91–100. https://doi.org/10.1016/j.materresbull.2016.01.027.

[123]. Li, J.; Li, J.-G.; Liu, S.; Li, X.; Sun, X.; Sakka, Y. Greatly Enhanced Dy^{3+} Emission via Efficient Energy Transfer in Gadolinium Aluminate Garnet ($Gd_3Al_5O_{12}$) Stabilized with Lu^{3+}. *J. Mater. Chem. C* **2013**, *1* (45), 7614. https://doi.org/10.1039/c3tc31413h.

[124]. Anilkumar, K.; Damodaraiah, S.; Babu, S.; Prasad, V. R.; Ratnakaram, Y. C. Emission Spectra and Energy Transfer Studies in Dy^{3+} and Dy^{3+}/Eu^{3+} Co-Doped Potassium Fluorophosphate Glasses for White Light Applications. *J. Lumin.* **2019**, *205*, 190–196. https://doi.org/10.1016/j.jlumin.2018.09.007.

[125]. Kolesnikov, I. E.; Kalinichev, A. A.; Kurochkin, M. A.; Golyeva, E. V.; Terentyeva, A. S.; Kolesnikov, E. Y.; Lähderanta, E. Structural, Luminescence and Thermometric Properties of Nanocrystalline YVO4:Dy^{3+} Temperature and Concentration Series. *Sci. Rep*. **2019**, *9 (1),* 2043. https://doi.org/10.1038/s41598-019-38774-6.

[126]. Uma, V.; Marimuthu, K.; Muralidharan, G. Influence of Modifier Cations on the Spectroscopic Properties of Dy^{3+} Doped Telluroborate Glasses for White Light Applications. *J. Fluores*c. **2016**, *26 (6),* 2281–2294. https://doi.org/10.1007/s10895-016-1924-y.

[127]. Lone, I. U. N.; M. Sirajuddeen , M. M. S.; Saubia, S.B. ; Khalid, S. A density functional calculations on electronic, magnetic, optical, mechanical and half-metallic

properties in molybdenum based pnictogens in GGA and GGA+U approach. *Mater. Chem. Phys.* **2021**, *260*, 124159. https://doi.org/10.1016/j.matchemphys.2020.124159

[128]. Brese, N. E.; O'Keeffe, M. Bond-valence parameters for solids. *Acta Crystallogr., Sect. B: Struct. Sci.,* **1991**, *47*, 192–197. https://doi.org/10.1107/S0108768190011041

[129]. Cicirello, G.; Wang, M.; Sam, Q. P.; Hart, J. L.; Williams, N. L.; Yin, H.; Cha, J. J.; Wang, J. Two-Dimensional Violet Phosphorus P_{11}: A Large Band Gap Phosphorus Allotrope. *J. Am. Chem. Soc.* **2023**, *145 (14),* 8218–8230. https://doi.org/10.1021/jacs.3c01766.

[130]. Maggard, P. A.; Stern, C. L.; Poeppelmeier, K. R. Understanding the Role of Helical Chains in the Formation of Noncentrosymmetric Solids. *J. Am. Chem. Soc.* **2001**, *123* (31), 7742–7743. https://doi.org/10.1021/ja016055y.

[131]. Marvel, M. R.; Lesage, J.; Baek, J.; Halasyamani, P. S.; Stern, C. L.; Poeppelmeier, K. R. Cation-Anion Interactions and Polar Structures in the Solid State. *J. Am. Chem. Soc.* **2007**, *129* (45), 13963–13969. https://doi.org/10.1021/ja074659h.

[132]. Mutailipu, M.; Zhang, M.; Yang, Z.; Pan, S. Targeting the next Generation of Deep-Ultraviolet Nonlinear Optical Materials: Expanding from Borates to Borate Fluorides to Fluorooxoborates. *Acc. Chem. Res.* **2019**, *52*, 791– 801, DOI: 10.1021/acs.accounts.8b00649

[133]. Kaidalova, T.A.; Pakhomov, V.I.; Panin, E.S. On the Structure of the $K_5Nb_3O_3F_{14}\cdot H_2O$ Crystal. *Koord. Khim*. **1976**, *2*, 554-556.

[134]. Udovenko, A.A.; Laptash, N.M. Dinuclear oxofluorometallates as a new structural type of d^0 transition metal oxofluoride compound. *Acta Crystallogr., Sect. B.* **2012**, *68*, 602-609. https://doi.org/10.1107/S0108768112042577

[135]. Holland, M.; Donakowski, M. D.; Pozzi, E. A.; Rasmussen, A. M.; Tran, T. T.; Pease-Dodson, S. E.; Halasyamani, P. S.; Seideman, T.; Van Duyne, R. P.; Poeppelmeier, K. R. Polar Alignment of Λ-Shaped Basic Building Units within Transition Metal Oxide Fluoride Materials. *Inorg. Chem*. **2014**, *53 (1),* 221–228. https://doi.org/10.1021/ic402177j.

[136]. Yu, H.; Nisbet, M. L.; Poeppelmeier, K. R. Assisting the Effective Design of Polar Iodates with Early Transition-Metal Oxide Fluoride Anions. *J. Am. Chem. Soc*. **2018**, *140 (28),* 8868–8876. https://doi.org/10.1021/jacs.8b04762.

[137]. Li, Q.; Liu, H.; Yu, H.; Hu, Z.; Wang, J.; Wu, Y.; Wu, H. Alignment of Λ-Shaped Basic Building Units to Construct One New $KMoO_3(IO_3)$ Polar Polymorph. *Inorg. Chem*. **2023**, *62 (9),* 3896–3903. https://doi.org/10.1021/acs.inorgchem.2c04282.

[138]. Chemingui, S.; Ferhi, M.; Horchani-Naifer, K.; Férid, M. Synthesis and Luminescence Characteristics of Dy^{3+} Doped $KLa(PO_3)_4$. *J. Lumin*. **2015**, *166,* 82–87. https://doi.org/10.1016/j.jlumin.2015.05.018.

For table of contents only:

Heteroanionic $LaBrWO_4$ achieves excellent second harmonic generation response and photoluminescent properties, which originates form the distortion of lambda (Λ)-shaped one-dimensional $[WO_5]$ strands.